An optimal adiabatic-to-diabatic transformation of the $1\,^2A'$ and $2\,^2A'$ states of H_3

Ravinder Abrol[a] and Aron Kuppermann[b]
Arthur Amos Noyes Laboratory of Chemical Physics, Division of Chemistry and Chemical Engineering, California Institute of Technology, Pasadena, California 91125

(Received 31 July 2001; accepted 1 October 2001)

Molecular reaction dynamics in the adiabatic representation is complicated by the existence of conical intersections and the associated geometric phase effect. The first-derivative coupling vector between the corresponding electronically adiabatic states can, in general, be decomposed into longitudinal (*removable*) and transverse (*nonremovable*) parts. At intersection geometries, the longitudinal part is singular, whereas the transverse part is not. In a two-electronic-state Born–Huang expansion, an adiabatic-to-diabatic transformation completely eliminates the contribution of the longitudinal part to the nuclear motion Schrödinger equation, leaving however the transverse part contribution. We report here the results of an accurate calculation of this transverse part for the $1\,^2A'$ and $2\,^2A'$ electronic states of H_3 obtained by solving a three-dimensional Poisson equation over the entire domain U of internal nuclear configuration space $\mathcal{Q}$ of importance to reactive scattering. In addition to requiring a knowledge of the first-derivative coupling vector everywhere in U, the solution depends on an arbitrary choice of boundary conditions. These have been picked so as to minimize the average value over U of the magnitude of the transverse part, resulting in an optimal diabatization angle. The dynamical importance of the transverse term in the diabatic nuclear motion Schrödinger equation is discussed on the basis of its magnitude not only in the vicinity of the conical intersection, but also over all of the energetically accessible regions of the full U domain. We also present and discuss the diabatic potential energy surfaces obtained by this optimal diabatization procedure. © *2002 American Institute of Physics.* [DOI: 10.1063/1.1419257]

I. INTRODUCTION

A detailed review of the adiabatic and diabatic representation of polyatomic molecules is given elsewhere[1] and we will only summarize below the main aspects needed for the present paper. We neglect all spin–spin and spin–orbit terms in the molecular Hamiltonian. Consider a polyatomic system with electronic coordinates $\mathbf{r}$ and nuclear coordinates $\mathbf{R}$. The total wave function for this system is given by the Born–Huang expansion[2,3]

$$\Psi(\mathbf{r},\mathbf{R})=\sum_n \chi_n^{\mathrm{ad}}(\mathbf{R})\,\psi_n^{\mathrm{ad}}(\mathbf{r};\mathbf{R}), \tag{1}$$

where $\psi_n^{\mathrm{ad}}(\mathbf{r};R)$ are the adiabatic electronic wave functions satisfying the electronic Schrödinger equation,

$$\hat{H}^{\mathrm{el}}(\mathbf{r};\mathbf{R})\,\psi_n^{\mathrm{ad}}(\mathbf{r};\mathbf{R})=\varepsilon_n^{\mathrm{ad}}(\mathbf{R})\,\psi_n^{\mathrm{ad}}(\mathbf{r};\mathbf{R}), \tag{2}$$

n is a complete set of quantum numbers needed to specify them and $\chi_n^{\mathrm{ad}}(\mathbf{R})$ are the adiabatic nuclear wave functions. $\varepsilon_n^{\mathrm{ad}}(\mathbf{R})$ are the electronically adiabatic potential energy surfaces (PESs). If two of these surfaces, labeled $n=i$ and $n=j$, exhibit a single conical intersection and the ψ_n^{ad} are required to be real, then according to the geometric phase (GP) theorem,[4–8]

$$\psi_n^{\mathrm{ad}}(\mathbf{r};\mathbf{R})\rightarrow -\psi_n^{\mathrm{ad}}(\mathbf{r};\mathbf{R}) \quad n=i,j \tag{3}$$

and

$$\chi_n^{\mathrm{ad}}(\mathbf{R})\rightarrow -\chi_n^{\mathrm{ad}}(\mathbf{R}) \quad n=i,j, \tag{4}$$

when the polyatomic system traverses a closed loop in nuclear configuration space $\mathcal{Q}$ around that conical intersection (a so called pseudo-rotation). As a result, the $\psi_n^{\mathrm{ad}}(\mathbf{r};\mathbf{R})$ are not single-valued functions of $\mathbf{R}$. Alternatively, if the electronic wave functions are allowed to be complex, they may be required to be single-valued.[9] For example, we may express them as

$$\overline{\psi}_n^{\mathrm{ad}}(\mathbf{r};\mathbf{R})=e^{iA_n(\mathbf{R})}\psi_n^{\mathrm{ad}}(\mathbf{r};\mathbf{R}) \quad n=i,j \tag{5}$$

and require that the $e^{iA_n(\mathbf{R})}$ $(n=i,j)$ change sign [i.e., that $A_n(\mathbf{R})$ change by π] upon a pseudorotation. The $A_n(\mathbf{R})$ are the geometric phases that appear in the corresponding modified adiabatic nuclear motion Schrödinger equation.[1,8–11] In the present paper, we will require the electronic wave functions to be real.

In a two-electronic-state representation of the system involving electronically adiabatic states i and j, Eq. (1) is written as

$$\Psi(\mathbf{r},\mathbf{R})=\chi_i^{\mathrm{ad}}(\mathbf{R})\,\psi_i^{\mathrm{ad}}(\mathbf{r};\mathbf{R})+\chi_j^{\mathrm{ad}}(\mathbf{R})\,\psi_j^{\mathrm{ad}}(\mathbf{r};\mathbf{R}). \tag{6}$$

Let us define $\boldsymbol{\chi}^{\mathrm{ad}}(\mathbf{R})$ as a two-dimensional column vector whose components are $\chi_i^{\mathrm{ad}}(\mathbf{R})$ and $\chi_j^{\mathrm{ad}}(\mathbf{R})$. The Schrödinger equation satisfied by $\boldsymbol{\chi}^{\mathrm{ad}}(\mathbf{R})$ is

[a]Work done in partial fulfillment of requirements for a Ph.D. degree in Chemistry.

[b]Author to whom correspondence should be addressed. Electronic mail: aron@caltech.edu

$$\left[-\frac{\hbar^2}{2\mu}\{\mathbf{I}\nabla_{\mathbf{R}}^2+2\mathbf{W}^{(1)\mathrm{ad}}(\mathbf{q})\cdot\nabla_{\mathbf{R}}+\mathbf{W}^{(2)\mathrm{ad}}(\mathbf{q})\}\right.$$

$$\left.+\{\boldsymbol{\varepsilon}^{\mathrm{ad}}(\mathbf{q})-E\mathbf{I}\}\right]\boldsymbol{\chi}^{\mathrm{ad}}(\mathbf{R})=\mathbf{0}, \tag{7}$$

where $\mathbf{q}$ represents a set of internal nuclear coordinates of the system, whereas $\mathbf{R}$ includes both $\mathbf{q}$ and the external coordinates that orient the system in space, but excludes the system's center-of-mass coordinates. The $\mathbf{R}$ symbol represents a set of nuclear coordinates that locate the N nuclei of the molecule in a center-of-mass frame, and μ is an overall reduced mass. $\mathbf{I}$, $\mathbf{W}^{(1)\mathrm{ad}}$, $\mathbf{W}^{(2)\mathrm{ad}}$, and $\boldsymbol{\varepsilon}^{\mathrm{ad}}$ are 2×2 matrices and $\nabla_{\mathbf{R}}$ is a gradient operator in the $3(N-1)$-dimensional nuclear configuration space. $\mathbf{I}$ is the identity matrix and $\boldsymbol{\varepsilon}^{\mathrm{ad}}$ is the diagonal matrix whose diagonal elements are the potential energy surfaces (PESs) $\varepsilon_i^{\mathrm{ad}}$ and $\varepsilon_j^{\mathrm{ad}}$ of the two electronically adiabatic states being considered. The matrices $\mathbf{W}^{(1)\mathrm{ad}}$ and $\mathbf{W}^{(2)\mathrm{ad}}$ are the first- and second-derivative[1,12–17] 2×2 coupling matrices whose elements are defined by

$$\left.\begin{aligned}\mathbf{W}_{m,n}^{(1)\mathrm{ad}}(\mathbf{q})&=\langle\psi_m^{\mathrm{ad}}(\mathbf{r};\mathbf{q})|\nabla_{\mathbf{R}}\psi_n^{\mathrm{ad}}(\mathbf{r};\mathbf{q})\rangle_{\mathbf{r}}\\ \mathrm{W}_{m,n}^{(2)\mathrm{ad}}(\mathbf{q})&=\langle\psi_m^{\mathrm{ad}}(\mathbf{r};\mathbf{q})|\nabla_{\mathbf{R}}^2\psi_n^{\mathrm{ad}}(\mathbf{r};\mathbf{q})\rangle_{\mathbf{r}}\end{aligned}\right\}m,n=i,j \tag{8}$$

and are, respectively, $3(N-2)$-dimensional vectors $[\mathbf{W}_{m,n}^{(1)\mathrm{ad}}(\mathbf{q})]$[18] and ordinary scalars $(\mathrm{W}_{m,n}^{(2)\mathrm{ad}}(\mathbf{q}))$. The matrix $\mathbf{W}^{(1)\mathrm{ad}}$ is in general skew-Hermitian and, due to the requirement that the ψ_n^{ad} be real, is real and skew-symmetric and can be written as

$$\mathbf{W}^{(1)\mathrm{ad}}(\mathbf{q})=\begin{pmatrix}0 & \mathbf{W}_{1,2}^{(1)\mathrm{ad}}(\mathbf{q})\\ -\mathbf{W}_{1,2}^{(1)\mathrm{ad}}(\mathbf{q}) & 0\end{pmatrix}. \tag{9}$$

For a triatomic system, $\mathbf{W}_{1,2}^{(1)\mathrm{ad}}$ is a three-dimensional vector that from here on will be labeled $\mathbf{w}^{(1)\mathrm{ad}}$. As any three-dimensional vector, it can be expressed, according to the Helmholtz theorem,[19] as a sum of a longitudinal part $\mathbf{w}_{\mathrm{lon}}^{(1)\mathrm{ad}}(\mathbf{q})$ and a transverse one $\mathbf{w}_{\mathrm{tra}}^{(1)\mathrm{ad}}(\mathbf{q})$ according to

$$\mathbf{w}^{(1)\mathrm{ad}}(\mathbf{q})=\mathbf{w}_{\mathrm{lon}}^{(1)\mathrm{ad}}(\mathbf{q})+\mathbf{w}_{\mathrm{tra}}^{(1)\mathrm{ad}}(\mathbf{q}), \tag{10}$$

where, by definition, the curl of $\mathbf{w}_{\mathrm{lon}}^{(1)\mathrm{ad}}(\mathbf{q})$ and the divergence of $\mathbf{w}_{\mathrm{tra}}^{(1)\mathrm{ad}}(\mathbf{q})$ vanish,

$$\nabla_{\mathbf{q}}\times\mathbf{w}_{\mathrm{lon}}^{(1)\mathrm{ad}}(\mathbf{q})=0, \tag{11}$$

$$\nabla_{\mathbf{q}}\cdot\mathbf{w}_{\mathrm{tra}}^{(1)\mathrm{ad}}(\mathbf{q})=0. \tag{12}$$

As a result of these equations, a scalar potential $\beta(\mathbf{q})$ and a vector potential $\mathbf{A}(\mathbf{q})$ [not to be confused with the scalar geometric phase $A_n(\mathbf{q})$ of Eq. (5)] exist for which

$$\mathbf{w}_{\mathrm{lon}}^{(1)\mathrm{ad}}(\mathbf{q})=\nabla_{\mathbf{q}}\beta(\mathbf{q}) \tag{13}$$

and

$$\mathbf{w}_{\mathrm{tra}}^{(1)\mathrm{ad}}(\mathbf{q})=\nabla_{\mathbf{q}}\times\mathbf{A}(\mathbf{q}). \tag{14}$$

At conical intersection geometries, $\mathbf{w}_{\mathrm{lon}}^{(1)\mathrm{ad}}(\mathbf{q})$ is singular because of the $\mathbf{q}$ dependence of $\psi_i^{\mathrm{ad}}(\mathbf{r};\mathbf{q})$ and $\psi_j^{\mathrm{ad}}(\mathbf{r};\mathbf{q})$ in their vicinity[18] and therefore so is the $\mathbf{W}^{(1)\mathrm{ad}}(\mathbf{q})\cdot\nabla_{\mathbf{R}}$ term in Eq. (7). For the same reason, $\mathrm{W}_{1,1}^{(2)\mathrm{ad}}(\mathbf{q})$ and $\mathrm{W}_{2,2}^{(2)\mathrm{ad}}(\mathbf{q})$ are also singular at such geometries. Replacing Eq. (10) into Eq. (9), $\mathbf{W}^{(1)\mathrm{ad}}$ can be written as a sum of the corresponding skew-symmetric matrices $\mathbf{W}_{\mathrm{lon}}^{(1)\mathrm{ad}}$ and $\mathbf{W}_{\mathrm{tra}}^{(1)\mathrm{ad}}$. In addition, the presence of a gradient term of this type, even if not singular (for intersections that are not conical or for nearly avoided intersections), introduces inefficiencies in the numerical solution of that equation. This makes it desirable to switch to a diabatic electronic basis,[1,20,21] $\psi_n^d(\mathbf{r};\mathbf{R})$, which in the two-electronic-state case is given by

$$\begin{pmatrix}\psi_i^d(\mathbf{r};\mathbf{R})\\ \psi_j^d(\mathbf{r};\mathbf{R})\end{pmatrix}=\tilde{\mathbf{U}}[\beta(\mathbf{q})]\begin{pmatrix}\psi_i^{\mathrm{ad}}(\mathbf{r};\mathbf{R})\\ \psi_j^{\mathrm{ad}}(\mathbf{r};\mathbf{R})\end{pmatrix} \tag{15}$$

where $\tilde{\mathbf{U}}[\beta(\mathbf{q})]$ is the transpose of the matrix,

$$\mathbf{U}[\beta(\mathbf{q})]=\begin{pmatrix}\cos\beta(\mathbf{q}) & -\sin\beta(\mathbf{q})\\ \sin\beta(\mathbf{q}) & \cos\beta(\mathbf{q})\end{pmatrix} \tag{16}$$

and $\beta(\mathbf{q})$ is called the diabatization or mixing angle. In terms of the diabatic electronic basis, Eq. (6) becomes

$$\Psi(\mathbf{r},\mathbf{R})=\chi_i^d(\mathbf{R})\psi_i^d(\mathbf{r};\mathbf{R})+\chi_j^d(\mathbf{R})\psi_j^d(\mathbf{r};\mathbf{R}), \tag{17}$$

where the relation between the $\chi_n^{\mathrm{ad}}(\mathbf{R})$ and $\chi_n^d(\mathbf{R})$ is

$$\boldsymbol{\chi}^d(\mathbf{R})=\tilde{\mathbf{U}}[\beta(\mathbf{q})]\boldsymbol{\chi}^{\mathrm{ad}}(\mathbf{R}), \tag{18}$$

where, in analogy to $\boldsymbol{\chi}^{\mathrm{ad}}(\mathbf{R})$, $\boldsymbol{\chi}^d(\mathbf{R})$ is the two-dimensional column vector whose two elements are $\chi_i^d(\mathbf{R})$ and $\chi_j^d(\mathbf{R})$. Replacement of Eq. (18) into Eq. (7) yields the diabatic nuclear motion scattering equation

$$\left[-\frac{\hbar^2}{2\mu}\{\mathbf{I}\nabla_{\mathbf{R}}^2+2\mathbf{W}_{\mathrm{tra}}^{(1)\mathrm{ad}}(\mathbf{q})\cdot\nabla_{\mathbf{R}}+\mathbf{W}^{(2)d}(\mathbf{q})\}\right.$$

$$\left.+\{\boldsymbol{\varepsilon}^d(\mathbf{q})-E\mathbf{I}\}\right]\boldsymbol{\chi}^d(\mathbf{R})=\mathbf{0}. \tag{19}$$

The elements of the first-derivative $\mathbf{W}^{(1)d}(\mathbf{q})$ and second-derivative $\mathbf{W}^{(2)d}(\mathbf{q})$ coupling diabatic matrices are analogous to their adiabatic counterparts and given by Eq. (8) with the $\psi_n^{\mathrm{ad}}(n=i,j)$ replaced by the ψ_n^d. In addition, $\boldsymbol{\varepsilon}^d(\mathbf{q})$ is the 2×2 matrix defined by

$$\boldsymbol{\varepsilon}^d(\mathbf{q})=\tilde{\mathbf{U}}[\beta(\mathbf{q})]\boldsymbol{\varepsilon}^{\mathrm{ad}}(\mathbf{q})\mathbf{U}[\beta(\mathbf{q})]. \tag{20}$$

The adiabatic-to-diabatic transformation eliminates the poles in both the first- and second-derivative coupling matrices. $\mathbf{W}^{(1)d}(\mathbf{q})$ does not appear explicitly in Eq. (19) but is equal to $\mathbf{W}_{\mathrm{tra}}^{(1)\mathrm{ad}}(\mathbf{q})$, as can be shown by using Eq. (15) in the definition of $\mathbf{W}^{(1)d}(\mathbf{q})$ together with Eqs. (10)–(14). Elements of the diabatic matrix $\mathbf{W}^{(2)d}$ are usually small in the vicinity of a conical intersection and can be added to $\boldsymbol{\varepsilon}^d$ to give a corrected diabatic matrix. As can be seen, whereas in Eq. (7) $\mathbf{W}^{(1)\mathrm{ad}}$ contains both the singular matrix $\mathbf{W}_{\mathrm{lon}}^{(1)\mathrm{ad}}$ and the nonsingular one $\mathbf{W}_{\mathrm{tra}}^{(1)\mathrm{ad}}$, Eq. (19) contains only the latter. Nevertheless, the residual first-derivative coupling term $\mathbf{W}_{\mathrm{tra}}^{(1)\mathrm{ad}}\cdot\nabla_{\mathbf{R}}$ does not vanish.

A "perfect" diabatic basis would be one for which the first-derivative coupling $\mathbf{W}^{(1)d}$ vanishes.[22] From the above mentioned considerations, we conclude, as is well known,[1,23,24] that a "perfect" diabatic basis cannot exist for a polyatomic system (except when the complete infinite set of electronic adiabatic functions is included[23,27]), which means that $\mathbf{W}^{(1)\mathrm{ad}}(\mathbf{q})$ cannot be transformed away to zero. As a result, the longitudinal and transverse parts of the first-derivative coupling vector are referred to as *removable* and

nonremovable parts, respectively. Over the years, a number of formulations of approximate or quasidiabatic or ''locally rigorous'' diabatic states[20,25–33] have appeared. Only very recently[34–39] have there been attempts to use high quality *ab initio* wave functions to consider the magnitude of the *nonremovable* part of the first-derivative coupling vector. In one such attempt,[38] a quasidiabatic basis was reported for the HeH_2 system by solving a two-dimensional Poisson equation on the plane in three-dimensional configuration space passing through the conical intersection configuration of smallest energy. It seems that no attempt has been made to get an optimal diabatization over the entire configuration space for a triatomic system, to facilitate accurate two-electronic-state scattering dynamics calculations. Conical intersections being omnipresent, such scattering calculations will permit a test of the validity of the one-electronic-state Born–Oppenheimer approximation as a function of energy in the presence of conical intersections, by comparing the results of these two kinds of calculations.

We report here an approach to obtain an optimal diabatic basis over the entire internal nuclear configuration space, based on the knowledge of the first-derivative coupling vector over the entire dynamically-important part U of that space and appropriately chosen boundary conditions. We have applied this approach to the simplest triatomic system, H_3, which has a conical intersection between the $1\,^2A'$ and $2\,^2A'$ electronic PESs at equilateral triangle geometries. The corresponding conical intersection line induces a geometric phase effect, important for the reaction properties of the ground electronic state.[1,40–46] The lowest conical intersection configuration energy occurs at 2.75 eV.[47] As a result, for energies in the vicinity of this value and above, the one-electronic-state Born–Oppenheimer approximation breaks down and a scattering calculation involving both these states and their couplings must be used to obtain accurate scattering results for this system. In this approach, first an adiabatic-to-diabatic transformation is obtained by calculating the diabatization angle $\beta(\mathbf{q})$ [appearing in Eq. (16)] from the first-derivative couplings $[\mathbf{W}^{(1)\mathrm{ad}}(\mathbf{q})]$. This calculation involves solving a three-dimensional Poisson equation with boundary conditions that minimize the average value of the magnitude of $\mathbf{W}^{(1)\mathrm{ad}}_{\mathrm{tra}}$ over U. This will allow an initial neglect of the term containing $\mathbf{W}^{(1)\mathrm{ad}}_{\mathrm{tra}}$ in Eq. (19) and a later reintroduction of this term followed by a solution using perturbative or other methods.

Another check of the existence of a nonzero transverse part $[\mathbf{W}^{(1)\mathrm{ad}}_{\mathrm{tra}}$ or equivalently $\mathbf{w}^{(1)\mathrm{ad}}_{\mathrm{tra}}]$ is the evaluation of line integrals of first-derivative couplings $\mathbf{w}^{(1)\mathrm{ad}}$ along loops around conical intersection geometries. If these integrals are carried along open paths $\mathcal{L}$ in nuclear configuration space, an angular potential $\Phi(\mathbf{q},\mathbf{q_0};\mathcal{L})$ with $\mathbf{q}\neq\mathbf{q_0}$ can be defined by[23,34,48,18]

$$\Phi(\mathbf{q},\mathbf{q_0};\mathcal{L})=\int_{\mathcal{L}\,\mathbf{q_0}}^{\mathbf{q}}\mathbf{w}^{(1)\mathrm{ad}}(\mathbf{q}')\cdot d\mathbf{q}', \tag{21}$$

where $\mathbf{q_0}$ locates the initial point on $\mathcal{L}$. This angle is called the open path phase.[49] It is also convenient to define the corresponding closed path phase Φ_{T}, called the topological phase,[50]

$$\Phi_{\mathsf{T}}(\mathcal{L})=\oint_{\mathcal{L}}\mathbf{w}^{(1)\mathrm{ad}}(\mathbf{q}')\cdot d\mathbf{q}'. \tag{22}$$

In light of Eq. (10), we can define two more angular potentials $\Phi_{\mathrm{lon}}(\mathbf{q},\mathbf{q_0};\mathcal{L})$ and $\Phi_{\mathrm{tra}}(\mathbf{q},\mathbf{q_0};\mathcal{L})$, by replacing $\mathbf{w}^{(1)\mathrm{ad}}$ in Eq. (21) by $\mathbf{w}^{(1)\mathrm{ad}}_{\mathrm{lon}}$ and $\mathbf{w}^{(1)\mathrm{ad}}_{\mathrm{tra}}$, respectively. The corresponding topological phases $\Phi_{\mathsf{T},\mathrm{lon}}(\mathcal{L})$ and $\Phi_{\mathsf{T},\mathrm{tra}}(\mathcal{L})$ can be likewise defined using Eq. (22) in lieu of Eq. (21),

$$\Phi_{\mathsf{T},\mathrm{lon}}(\mathcal{L})=\oint_{\mathcal{L}}\mathbf{w}^{(1)\mathrm{ad}}_{\mathrm{lon}}(\mathbf{q}')\cdot d\mathbf{q}', \tag{23}$$

$$\Phi_{\mathsf{T},\mathrm{tra}}(\mathcal{L})=\oint_{\mathcal{L}}\mathbf{w}^{(1)\mathrm{ad}}_{\mathrm{tra}}(\mathbf{q}')\cdot d\mathbf{q}'. \tag{24}$$

According to the geometric phase theorem[7,34,35]

$$\Phi_{\mathsf{T},\mathrm{lon}}(\mathcal{L})=p\,\pi, \tag{25}$$

where $p=0$ if $\mathcal{L}$ does not enclose any conical intersection and $p=1$ if it encloses one conical intersection. Using this and Eq. (10) we have

$$\Phi_{\mathsf{T},\mathrm{tra}}(\mathcal{L})=\Phi_{\mathsf{T}}(\mathcal{L})-p\,\pi. \tag{26}$$

As a result, a necessary but insufficient condition for the first-derivative coupling to be purely longitudinal is that $\Phi_{\mathsf{T},\mathrm{tra}}(\mathcal{L})$ vanish.[38] Nonzero $\Phi_{\mathsf{T},\mathrm{tra}}(\mathcal{L})$ and hence a nonzero $\mathbf{w}^{(1)\mathrm{ad}}_{\mathrm{tra}}$ correspond to the existence of nonzero derivative couplings involving electronic states outside the two-electronic-state space[24] being considered in the present paper.

In Sec. II, we present an approach to obtain an optimal diabatic basis by using a Poisson equation obtained from Eqs. (10)–(12), similar to that used previously,[38] and a special set of boundary conditions. The present Poisson equation differs from the latter, however, in that it extends over the entire three-dimensional U domain of configuration space and uses very different boundary conditions. In Sec. III, we present the results of the diabatization angle calculation and the longitudinal as well as transverse parts of the first-derivative coupling vector and discuss the possible implications of dropping the transverse part in two-electronic-state quantum scattering calculations. The open-path phases Φ_{lon} and Φ_{tra} and topological (closed-path) phases $\Phi_{\mathsf{T},\mathrm{lon}}$ and $\Phi_{\mathsf{T},\mathrm{tra}}$ are evaluated, which confirm the presence of a nonzero transverse part. We also present the diabatic PESs [elements of the 2×2 diabatic energy matrix $\boldsymbol{\varepsilon}^{d}(\mathbf{q})$] corresponding to this optimal diabatic basis and discuss their features. In Sec. IV, we conclude with a summary and the future direction of this work.

II. METHODOLOGY

A. Coordinate system

For any triatomic system, the internal nuclear coordinate space $\mathcal{Q}$ spanned by $\mathbf{q}$ is three-dimensional. We adopt the symmetrized hyperspherical coordinates $\mathbf{q}\equiv(\rho,\theta,\phi_\lambda)$ used previously.[1,42–46,51] The ranges of these coordinates are as follows:

$$0\leqslant\rho<\infty,\quad 0\leqslant\theta\leqslant\pi/2,\quad 0\leqslant\phi_\lambda<2\pi. \tag{27}$$

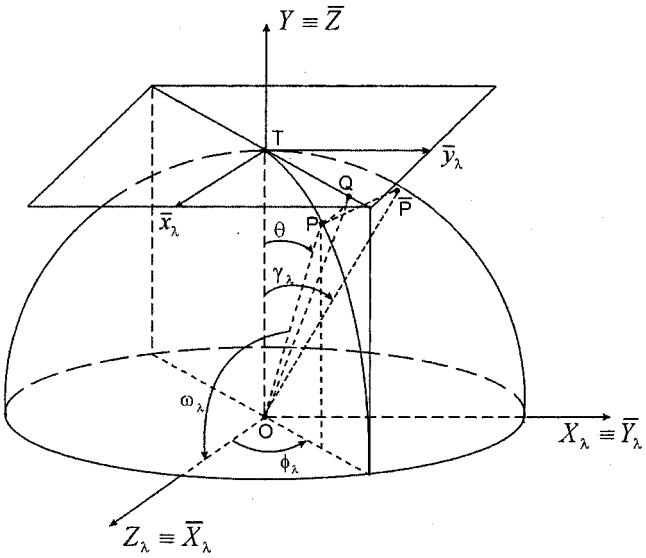

FIG. 1. Mapping of a point P of a constant ρ hemisphere in the $OX_\lambda YZ_\lambda$ space onto a point Q on a plane tangent to that hemisphere at the intersection T of the OY axis with it, such that the length of the arc(TP) = TQ. The point P has θ, ϕ_λ polar angles in the $O\bar{X}_\lambda\bar{Y}_\lambda\bar{Z}$ space and $\omega_\lambda, \gamma_\lambda$ in the $OX_\lambda YZ_\lambda$ space. $\bar{P}$ is the projection of point P on the $OX_\lambda Y$ plane.

For a constant hyperradius ρ, these coordinates span a hemisphere whereas ordinary spherical polar coordinates span a full sphere.

The H_3 system exhibits a conical intersection between the $1\,^2A'$ and $2\,^2A'$ electronic PESs for equilateral triangle geometries, which corresponds to $\theta = 0$ and all values of ρ and ϕ_λ. Collinear geometries of H_3 are mapped by $\theta = \pi/2$ for all values of ρ and ϕ_λ.

Projection plots of physical quantities in internal configuration space Cartesian coordinates $(X_\lambda, Y, Z_\lambda)$, which are related to these symmetrized hyperspherical coordinates, provide valuable information for reactive scattering calculations that use these physical quantities and hyperspherical coordinates. As mentioned above, for a constant hyperradius ρ the hyperspherical coordinates span a hemisphere. Figure 1 shows this hemisphere for a constant ρ (the radius of this hemisphere) and a point P on this hemisphere which has θ, ϕ_λ polar angles in the $O\bar{X}_\lambda\bar{Y}_\lambda\bar{Z}$ frame and another related set of polar angles $\omega_\lambda, \gamma_\lambda$ in the associated $OX_\lambda YZ_\lambda$ frame. $\gamma_\lambda = 0°$ or 180° (equivalent to $\theta = 90°$) corresponds to collinear configurations of the H_3 system and $\gamma_\lambda = 90°$ to configurations for which the H atom is on the perpendicular bisector of the H–H line. All these coordinates and their interrelations have been discussed elsewhere.[18,52–58]

B. The Poisson equation

Replacing Eq. (13) into Eq. (10) results in

$$\mathbf{w}^{(1)\mathrm{ad}}(\mathbf{q}) = \boldsymbol{\nabla}_{\mathbf{q}}\beta(\mathbf{q}) + \mathbf{w}_{\mathrm{tra}}^{(1)\mathrm{ad}}(\mathbf{q}), \tag{28}$$

where $\boldsymbol{\nabla}_{\mathbf{q}}$ is the gradient operator in the $O\bar{X}_\lambda\bar{Y}_\lambda\bar{Z}$ cartesian frame of Fig. 1. Taking the divergence of both sides of this equation and using Eq. (14) together with the known property that the divergence of a curl of a three-dimensional vector vanishes, we get

$$\nabla_{\mathbf{q}}^2\beta(\mathbf{q}) = \sigma(\mathbf{q}), \tag{29}$$

where

$$\sigma(\mathbf{q}) = \boldsymbol{\nabla}_{\mathbf{q}} \cdot \mathbf{w}^{(1)\mathrm{ad}}(\mathbf{q}) \tag{30}$$

is known because $\mathbf{w}^{(1)\mathrm{ad}}(\mathbf{q})$ has been accurately calculated and fitted over the entire $\mathcal{Q}$ space of interest.[18] Equation (29) is the Poisson equation for $\beta(\mathbf{q})$. Once the boundary conditions associated with it are chosen, this equation can be solved numerically. Replacing the solution into Eq. (28) then furnishes $\mathbf{w}_{\mathrm{tra}}^{(1)\mathrm{ad}}(\mathbf{q})$ and therefore the first-derivative transverse coupling matrix,

$$\mathbf{W}_{\mathrm{tra}}^{(1)\mathrm{ad}}(\mathbf{q}) = \begin{pmatrix} 0 & \mathbf{w}_{\mathrm{tra}}^{(1)\mathrm{ad}}(\mathbf{q}) \\ -\mathbf{w}_{\mathrm{tra}}^{(1)\mathrm{ad}}(\mathbf{q}) & 0 \end{pmatrix} \tag{31}$$

which appears in the diabatic nuclear motion scattering Eq. (19). As a result, the flexibility provided by the selection of these boundary conditions injects an element of flexibility in the determination of $\mathbf{W}_{\mathrm{tra}}^{(1)\mathrm{ad}}(\mathbf{q})$.

In the next section we discuss the nature of the effect of the boundary conditions on this determination and how to select these conditions so as to result in an optimal diabatization.

C. Boundary conditions for solving the Poisson equation

The Poisson equation [Eq. (29)], being a second-order partial differential equation, has an infinite set of solutions because of the infinite choice of boundary conditions that can be imposed on it. Any of these solutions results in a $\beta(\mathbf{q})$ that removes the singularity in $\mathbf{W}^{(1)\mathrm{ad}}(\mathbf{q})$ at the conical intersection geometries upon the adiabatic-to-diabatic transformation defined by Eqs. (18) and (16). If $\sigma(\mathbf{q})$ goes to zero at infinity, a formal solution that also goes to zero at infinity is[1,19,59]

$$\beta(\mathbf{q}) = -\int \frac{\sigma(\mathbf{q}')}{4\pi|\mathbf{q}-\mathbf{q}'|}\,d\mathbf{q}'. \tag{32}$$

This is, however, not the only boundary condition possible. To pick an optimal set of boundary conditions we need to look at the individual terms in the diabatic nuclear motion Schrödinger equation [Eq. (19)].

It is customary in two-electronic-state problems to introduce two approximations into this equation. The first is to assume that the $\mathbf{W}^{(2)d}(\mathbf{q})\boldsymbol{\chi}^d(\mathbf{R})$ term is negligible compared to the remaining ones. This term vanishes for a complete diabatic electronic basis set but not for a two-diabatic electronic basis set. The second is to assume that the $\mathbf{W}_{\mathrm{tra}}^{(1)\mathrm{ad}}(\mathbf{q}) \cdot \boldsymbol{\nabla}_{\mathbf{R}}\boldsymbol{\chi}^d(\mathbf{R})$ term is negligible compared to the remaining ones. This assumption is justifiable if $\mathbf{W}_{\mathrm{tra}}^{(1)\mathrm{ad}}(\mathbf{q})$ is sufficiently small in the entire internal nuclear configuration space $\mathcal{Q}$ and in particular in the neighborhood of the conical intersection. This suggests that we select the boundary conditions satisfied by Eq. (29) so as to minimize as much as possible this transverse part in this space.

We will select a domain V in configuration space $\mathcal{Q}$, enclosed by a boundary surface S, within which the Poisson equation is to be solved. This domain includes the dynamically important part of $\mathcal{Q}$. The definitions of V and S are given in Sec. II D. As shown in that section, the choice of a reference surface at which the adiabatic and diabatic wave functions are equal, together with the condition that the adiabatic-to-diabatic transformation should reflect the P_3 permutation symmetry of the H_3 system, as well as the change of sign under pseudorotations given by Eq. (4), fixes the value of $\beta(\mathbf{q})$ on parts of S. On the remaining parts, we pick the following boundary condition [using Eq. (28)]:

$$[\boldsymbol{\nabla}_{\mathbf{q}}\beta(\mathbf{q})]_{\mathsf{S}}=[\mathbf{w}^{(1)\mathrm{ad}}(\mathbf{q})]_{\mathsf{S}}. \tag{33}$$

The reason for this choice is that if we make the transverse part zero on some parts of the boundary surface S, Eq. (28) leads directly to Eq. (33) on those parts. This equation corresponds to a Neumann boundary condition for the Poisson equation and, as proven in the Appendix, minimizes the average value of the magnitude of this transverse part over the domain V. Using this condition tends to decrease the magnitude of the $\mathbf{W}_{\mathrm{tra}}^{(1)\mathrm{ad}}(\mathbf{q})\cdot\boldsymbol{\nabla}_{\mathbf{R}}\boldsymbol{\chi}^{d}(\mathbf{R})$ term in Eq. (19). This is therefore an optimal boundary condition. It is quite different from setting $\beta(\mathbf{q})=0$ at the boundary, as will be shown in Sec. II D. In order to assess the effect of $\mathbf{W}_{\mathrm{tra}}^{(1)\mathrm{ad}}$ on the dynamics, one can first solve Eq. (19) omitting that term and then reintroduce it using perturbation theory or other methods.

D. Numerical solution of the Poisson equation

We express the Poisson equation [Eq. (29)] in terms of the internal hyperspherical coordinates ρ,θ,ϕ_λ as

$$\left[\frac{\partial^2}{\partial\rho^2}+\frac{2}{\rho}\frac{\partial}{\partial\rho}+\frac{1}{\rho^2}\left(\frac{\partial^2}{\partial\theta^2}+\cot\theta\frac{\partial}{\partial\theta}+\frac{1}{\sin^2\theta}\frac{\partial^2}{\partial\phi_\lambda^2}\right)\right]\beta(\rho,\theta,\phi_\lambda)=\sigma(\rho,\theta,\phi_\lambda). \tag{34}$$

For the H_3 system, we change the dependent variable β to γ by the transformation,

$$\beta(\rho,\theta,\phi_\lambda)=\frac{\phi_\lambda}{2}-\gamma(\rho,\theta,3\phi_\lambda). \tag{35}$$

The dependence of γ on $3\phi_\lambda$ (rather than on ϕ_λ simply) is due to the P_3 permutation symmetry of the H_3 system. It should be noted that although the P_3 group is isomorphic with C_{3v}, the configurations we are considering are only equilateral triangles for $\theta=0°$. The term $\phi_\lambda/2$ is responsible for the singularity in the first-derivative coupling vector at conical intersection ($\theta=0°$) configurations. When ϕ_λ changes by 2π radians during a pseudo-rotation (which encircles the conical intersection), γ does not change but β changes by π. As pointed out in the beginning of the introduction, under such a pseudo-rotation $\boldsymbol{\chi}^{\mathrm{ad}}$ changes sign and as a result of Eqs. (18) and (16) $\boldsymbol{\chi}^{d}$ is unchanged and is single-valued. This is a useful property of the diabatic representation. An approximate analytical expression for $\beta(\rho,\theta,\phi_\lambda)$ was obtained by Varandas *et al.*[47] using a double many-body expansion (DMBE) of the two lowest electronic PESs for H_3, and is given by

$$\beta^{\mathrm{DMBE}}(\rho,\theta,\phi_\lambda)=\frac{\phi_\lambda}{2}-\gamma^{\mathrm{DMBE}}(\rho,\theta,3\phi_\lambda), \tag{36}$$

where

$$\gamma^{\mathrm{DMBE}}(\rho,\theta,3\phi_\lambda)=\frac{1}{2}\tan^{-1}\frac{g_0(\rho)\sin\theta\sin3\phi_\lambda}{f_0(\rho)+g_0(\rho)\sin\theta\cos3\phi_\lambda+f_1(\rho)\sin^2\theta} \tag{37}$$

and $g_0(\rho)$, $f_0(\rho)$, and $f_1(\rho)$ are functions that depend only on the hyperradius ρ. $\beta^{\mathrm{DMBE}}(\rho,\theta,\phi_\lambda)$ is accurate close to conical intersection geometries, i.e.,

$$\beta^{\mathrm{DMBE}}(\rho,\theta,\phi_\lambda)\underset{\theta\to0}{\rightarrow}\beta(\rho,\theta,\phi_\lambda). \tag{38}$$

In the DMBE treatment, the transverse part of the first-derivative coupling vector is assumed to be negligible (especially near the conical intersection) as compared to the longitudinal part. In this approximation $\mathbf{w}_{\mathrm{tra,DMBE}}^{(1)\mathrm{ad}}(\mathbf{q})$ is required to vanish at all $\mathbf{q}$, i.e.,

$$\mathbf{w}_{\mathrm{DMBE}}^{(1)\mathrm{ad}}(\mathbf{q})=\boldsymbol{\nabla}_{\mathbf{q}}\beta^{\mathrm{DMBE}}(\mathbf{q}). \tag{39}$$

To test the validity of Eq. (38), since we know $\beta^{\mathrm{DMBE}}(\rho,\theta,\phi_\lambda)$ analytically, we compared $\mathbf{w}_{\mathrm{DMBE}}^{(1)\mathrm{ad}}(\mathbf{q})$ with our *ab initio* first-derivative coupling vector $\mathbf{w}^{(1)\mathrm{ad}}(\mathbf{q})$ in regions near the conical intersection and found a systematic mismatch in sign that was removed by changing the sign of $g_0(\rho)$ in the DMBE code. After making this change these first-derivative coupling vectors agreed quite well in these regions. Rewriting the Poisson Eq. (34) in terms of $\gamma(\rho,\theta,3\phi_\lambda)$ by using Eq. (35) we get

$$-\left[\frac{\partial^2}{\partial\rho^2}+\frac{2}{\rho}\frac{\partial}{\partial\rho}+\frac{1}{\rho^2}\left(\frac{\partial^2}{\partial\theta^2}+\cot\theta\frac{\partial}{\partial\theta}+\frac{1}{\sin^2\theta}\frac{\partial^2}{\partial\phi_\lambda^2}\right)\right]\gamma(\rho,\theta,3\phi_\lambda)=\sigma(\rho,\theta,3\phi_\lambda). \tag{40}$$

This equation was solved using the MUDPACK[60,61] library of subroutines. This library permits the solution of two- and three-dimensional linear elliptic partial differential equations with any combination of periodic, Dirichlet (for which the unknown function is specified on the boundary), Neumann (for which a derivative of the unknown function at the boundary is specified), and mixed Dirichlet–Neumann boundary conditions. The solution of Eq. (40) was obtained on the following restricted domain V of nuclear configuration space:

$$1.5\ \text{bohr}\leqslant\rho\leqslant10\ \text{bohr},\quad 0.1°\leqslant\theta\leqslant90°,$$

$$0°\leqslant\phi_\lambda\leqslant60°. \tag{41}$$

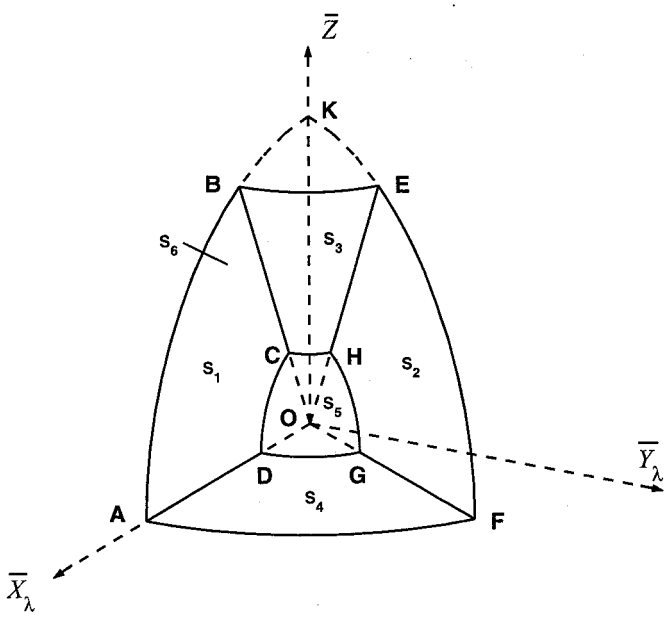

FIG. 2. Boundary surface S for solving the Poisson Eq. (34) in the $O\overline{X}_\lambda\overline{Y}_\lambda\overline{Z}$ space of Fig. 1. The surface is not drawn to exact scale. Arc(DG) is part of a circle of radius 1.5 bohr; arc(AF) is part of a circle of radius 10 bohr; $\angle AOF=60°$; and $\angle BOK=\angle EOK=0.1°$. The surface S is composed of 6 parts: ABCD surface S_1 ($\phi_\lambda=0°$, $0.1°\leqslant\theta\leqslant90°$, 1.5 bohr$\leqslant\rho\leqslant$10 bohr); EFGH surface S_2 ($\phi_\lambda=60°$, $0.1°\leqslant\theta\leqslant90°$, 1.5 bohr$\leqslant\rho\leqslant$10 bohr); BCHE surface S_3 ($\theta=0.1°$, $0°\leqslant\phi_\lambda\leqslant60°$, 1.5 bohr$\leqslant\rho\leqslant$10 bohr); ADGF surface S_4 ($\theta=90°$, $0°\leqslant\phi_\lambda\leqslant60°$, 1.5 bohr$\leqslant\rho\leqslant$10 bohr); CDGH surface S_5 ($\rho=1.5$ bohr, $0.1°\leqslant\theta\leqslant90°$, $0°\leqslant\phi_\lambda\leqslant60°$); and ABEF surface S_6 ($\rho=10$ bohr, $0.1°\leqslant\theta\leqslant90°$, $0°\leqslant\phi_\lambda\leqslant60°$).

The full domain $U\equiv6V$ has the same ρ and θ ranges as in Eq. (41) but the full ϕ_λ range of 0° to 360°. The solution over V leads directly to a solution over U with the help of the P_3 symmetry properties of the system. The use of 1.5 bohr for the minimum value of ρ required a small extrapolation of the *ab initio* first-derivative couplings available in the 2 bohr to 8 bohr interval. At 2 bohr, the lowest energy point on the ground adiabatic DSP PES[18] is about 3 eV. The corresponding lowest energy point for $\rho=1.5$ bohr is greater than 5 eV and hence regions of configuration space for which $\rho<1.5$ bohr (very compact nuclear geometries) will not be important for scattering dynamics at energies less than 5 eV, approximately. The 10 bohr value was chosen as the maximum ρ because at this hyperradius the H + H_2 interaction energy is too small to affect reaction cross sections of interest to this paper. The lowest value used for θ was 0.1° because the Poisson equation solver in the MUDPACK library for spherical polar coordinates is unstable for values of θ below that value. Besides, at such small values of θ, both β and γ are known since the DMBE representation[47] [Eqs. (36) and (37)] is quite accurate in these regions.

Let us consider the internal configuration space frame $O\overline{X}_\lambda\overline{Y}_\lambda\overline{Z}$ of Fig. 1 in which an internal nuclear configuration **q** is represented by a point whose spherical polar coordinates are ρ, θ, ϕ_λ. Figure 2 depicts in this frame the boundary surface S that encloses the domain V defined by Eq. (41). It is comprised of six pieces:

(a) S_1, the surface defined by $\phi_\lambda=0°$, $0.1°\leqslant\theta\leqslant90°$, and 1.5 bohr$\leqslant\rho\leqslant$10 bohr. It lies on the positive $\overline{X}_\lambda$ and $\overline{Z}$ quadrant of the $O\overline{X}_\lambda\overline{Z}$ plane. Its vertices are points A, B, C, and D.

(b) S_2, the surface defined by $\phi_\lambda=60°$, $0.1°\leqslant\theta\leqslant90°$, and 1.5 bohr$\leqslant\rho\leqslant$10 bohr. It is analogous to S_1, but lies on a plane containing the $O\overline{Z}$ axis and making an angle of 60° with the $O\overline{X}_\lambda\overline{Z}$ plane (measured counterclockwise from the latter as viewed from a point on the $O\overline{Z}$ axis having $\overline{Z}>0$). Its vertices are points E, F, G, and H.

(c) S_3, the surface defined by $\theta=0.1°$, $0°\leqslant\phi\leqslant60°$ and 1.5 bohr$\leqslant\rho\leqslant$10 bohr. It is a piece of a narrow conical surface whose vertices are B, C, H, and E.

(d) S_4, the surface defined by $\theta=90°$, $0°\leqslant\phi\leqslant60°$ and 1.5 bohr$\leqslant\rho\leqslant$10 bohr. It lies on the $O\overline{X}_\lambda\overline{Y}_\lambda$ plane. Its vertices are A, D, G, and F.

(e) S_5, the surface defined by $\rho=1.5$ bohr, $0.1°\leqslant\theta\leqslant90°$, and $0°\leqslant\phi\leqslant60°$. It is a portion of a spherical surface of radius 1.5 bohr having as edges the intersections with S_1, S_2, S_3, and S_4. Its vertices are C, D, G, and H.

(f) S_6, the surface defined by $\rho=10$ bohr, $0.1°\leqslant\theta\leqslant90°$, and $0°\leqslant\phi\leqslant60°$. It is a portion of a spherical surface of radius 10 bohr having as edges the intersections with S_1, S_2, S_3, and S_4. Its vertices are A, B, E, and F.

The boundary conditions adopted on S were the following:

(a) On S_1,

$$\beta(S_1)=\gamma(S_1)=0 \tag{42}$$

for all points on this surface. From Eqs. (16), (18), and (35), this condition results in the relation

$$\chi^d(S_1)=\chi^{ad}(S_1). \tag{43}$$

In other words, S_1 is chosen as the surface on which the diabatic and adiabatic representations coincide. This is a natural Dirichlet boundary condition.

(b) On S_2,

$$\beta(S_2)=\pi/6 \quad \text{and} \quad \gamma(S_2)=0 \tag{44}$$

for all points on this surface. This condition is a consequence of Eq. (42) and the P_3 symmetry of the H_3 system and forces γ to be single valued upon a pseudo-rotation of the system around the conical intersection line between the $1\,^2A'$ and $2\,^2A'$ states of H_3, i.e., to have the same value at $\phi_\lambda=0°$ and $\phi_\lambda=360°$. This in turn forces $\beta(\rho,\theta,\phi_\lambda)$ [Eq. (35)] to change by π upon such a pseudorotation, as required. This is also a natural Dirichlet boundary condition that follows from the one on S_1.

(c) On S_3,

$$\beta(S_3)=\phi_\lambda/2 \ \text{ and } \ \gamma(S_3)=0 \tag{45}$$

for all points on this surface. This is a consequence of the fact that, close to the conical intersection ($\theta=0.1°$ in the present case), the electronic wave functions $\psi_i^{ad}(\mathbf{r};\mathbf{q})$ and

$\psi_j^{\mathrm{ad}}(\mathbf{r};\mathbf{q})$ are, to first order in θ, independent of θ and depend on $\mathbf{q}$ only through ρ and ϕ_λ.[1] This is a mandatory Dirichlet boundary condition.

For boundary surfaces S_4 through S_6 we chose Neumann boundary conditions which force the θ-component of $\mathbf{w}_{\mathrm{tra}}^{(1)\mathrm{ad}}$ to vanish at the S_4 boundary and the ρ-component of this vector to vanish at the S_5 and S_6 boundaries. As proven in the Appendix, these choices minimize the average value of the magnitude of $\mathbf{w}_{\mathrm{tra}}^{(1)\mathrm{ad}}$ over the space enclosed by S. Specifically, the boundary conditions on S_4 through S_6 are

(d) On S_4,

$$\left(\frac{\partial\beta}{\partial\theta}\right)_{S_4} = -\left(\frac{\partial\gamma}{\partial\theta}\right)_{S_4} = \rho\, \mathrm{w}_\theta^{(1)\mathrm{ad}}(\rho,\theta=90^\circ,\phi_\lambda) \tag{46}$$

for all points on this surface. This condition results in the property

$$\mathrm{w}_{\mathrm{tra},\theta}^{(1)\mathrm{ad}}(\rho,\theta=90^\circ,\phi_\lambda)=0, \tag{47}$$

i.e., the θ-component of $\mathbf{w}_{\mathrm{tra}}^{(1)\mathrm{ad}}$ is forced to vanish on this surface.

(e) On S_5,

$$\left(\frac{\partial\beta}{\partial\rho}\right)_{S_5} = -\left(\frac{\partial\gamma}{\partial\rho}\right)_{S_5} = \mathrm{w}_\rho^{(1)\mathrm{ad}}(\rho=1.5\,\mathrm{bohr},\theta,\phi_\lambda) \tag{48}$$

which results in

$$\mathrm{w}_{\mathrm{tra},\rho}^{(1)\mathrm{ad}}(\rho=1.5\,\mathrm{bohr},\theta,\phi_\lambda)=0. \tag{49}$$

(f) On S_6,

$$\left(\frac{\partial\beta}{\partial\rho}\right)_{S_6} = -\left(\frac{\partial\gamma}{\partial\rho}\right)_{S_6} = \mathrm{w}_\rho^{(1)\mathrm{ad}}(\rho=10\,\mathrm{bohr},\theta,\phi_\lambda) \tag{50}$$

which results in

$$\mathrm{w}_{\mathrm{tra},\rho}^{(1)\mathrm{ad}}(\rho=10\,\mathrm{bohr},\theta,\phi_\lambda)=0. \tag{51}$$

The calculation using the boundary conditions above will henceforth be designated as $\mathbf{b}_0$.

The number of grid points used in the ρ, θ, and ϕ_λ directions in the MUDPACK equation solver was 513, 257, and 65, respectively, for a total of about 8.6 million grid points. The relative number of points for the three variables was found to optimize the accuracy of the solution. The grid spacings associated with ρ and θ were smaller than that associated with ϕ_λ because the Neumann boundary conditions for S_4-S_6 and the associated evaluation of numerical derivatives required such finer grids.

$\gamma(\rho,\theta,3\phi_\lambda)$, obtained by the solution of the Poisson equation [Eq. (40)] with the boundary conditions just described, was used in Eq. (35) to obtain the diabatization angle, $\beta(\rho,\theta,\phi_\lambda)$. This angle was then used in Eq. (28) to obtain the transverse part of the first-derivative coupling vector. As a check of the self-consistency of the calculations performed, we also employed the values of γ obtained at the boundary surfaces S_4-S_6 as Dirichlet starting conditions in a new solution of the Poisson equation involving only Dirichlet conditions. As expected, the new results were identical to the previous ones within the numerical accuracy of the calculation.

To obtain a quantitative estimate of the sensitivity of the solution of the Poisson equation to the boundary conditions used, we generated solutions for the following additional sets of boundary conditions:

(1) Neumann conditions on S_3-S_6 and Dirichlet conditions on S_1 and S_2. The Neumann condition on S_3 is given by

$$\left(\frac{\partial\beta}{\partial\theta}\right)_{S_3} = -\left(\frac{\partial\gamma}{\partial\theta}\right)_{S_3} = \rho\, \mathrm{w}_\theta^{(1)\mathrm{ad}}(\rho,\theta=0.1^\circ,\phi_\lambda) \tag{52}$$

which results in the property

$$\mathrm{w}_{\mathrm{tra},\theta}^{(1)\mathrm{ad}}(\rho,\theta=0.1^\circ,\phi_\lambda)=0. \tag{53}$$

This property is consistent with the boundary condition Eq. (45) (at $\theta=0.1^\circ$ but not necessarily at other small θ) and as a result we should expect this calculation to yield results very close to those obtained in the $\mathbf{b}_0$ calculation. That did indeed turn out to be the case, the results of the two calculations differing only slightly near the conical intersection (for $\theta\lesssim 3^\circ$) and being identical (within calculation accuracy) away from it. The ratio ξ_1 defined by Eq. (55), differed from unity by less than 10^{-4}.

(2) Dirichlet conditions $\gamma=0$ on all six boundaries S_1-S_6. This calculation without any Neumann boundary condition is expected to give results that most differ from the optimal $\mathbf{b}_0$ (3 Dirichlet and 3 Neumann) boundary conditions.

(3) Neumann conditions on S_4 and S_5 and $\gamma=0$ Dirichlet conditions on the other S_i.

(4) Neumann conditions on S_4 and S_6 and $\gamma=0$ Dirichlet conditions on the other S_i.

(5) Neumann conditions on S_5 and S_6 and $\gamma=0$ Dirichlet conditions on the other S_i.

(6) Neumann conditions on S_4 and $\gamma=0$ Dirichlet conditions on the other S_i.

(7) Neumann conditions on S_5 and $\gamma=0$ Dirichlet conditions on the other S_i.

(8) Neumann conditions on S_6 and $\gamma=0$ Dirichlet conditions on the other S_i.

The Neumann conditions referred to in (3)–(8) above are those given by Eqs. (46), (48), and (50). The calculations specified in (1)–(8) above will henceforth be designated as $\mathbf{b}_1-\mathbf{b}_8$, respectively. They were all performed using the same grid parameters as for $\mathbf{b}_0$, described after Eq. (51).

In order to compare results of calculations $\mathbf{b}_0-\mathbf{b}_8$, we calculated for each the corresponding root-mean-square average magnitude of the transverse coupling vector, over the full domain U of configuration space, defined by

$$\langle \mathrm{w}_{\mathrm{tra}}^{(1)\mathrm{ad}}\rangle_i = \left[\frac{\int_U |\mathbf{w}_{\mathrm{tra}}^{(1)\mathrm{ad}}(\mathbf{q})|^2 d\mathbf{q}}{\int_U d\mathbf{q}}\right]^{1/2} \quad i=0-8, \tag{54}$$

where $d\mathbf{q}$ is the volume element of the domain U. We also obtained the ratios,

$$\xi_i = \frac{\langle \mathrm{w}_{\mathrm{tra}}^{(1)\mathrm{ad}}\rangle_i}{\langle \mathrm{w}_{\mathrm{tra}}^{(1)\mathrm{ad}}\rangle_0} \quad i=0-8 \tag{55}$$

which will be useful for comparing the results of these $\mathbf{b}_i$ calculations. The larger ξ_i is, the larger is the deviation of the

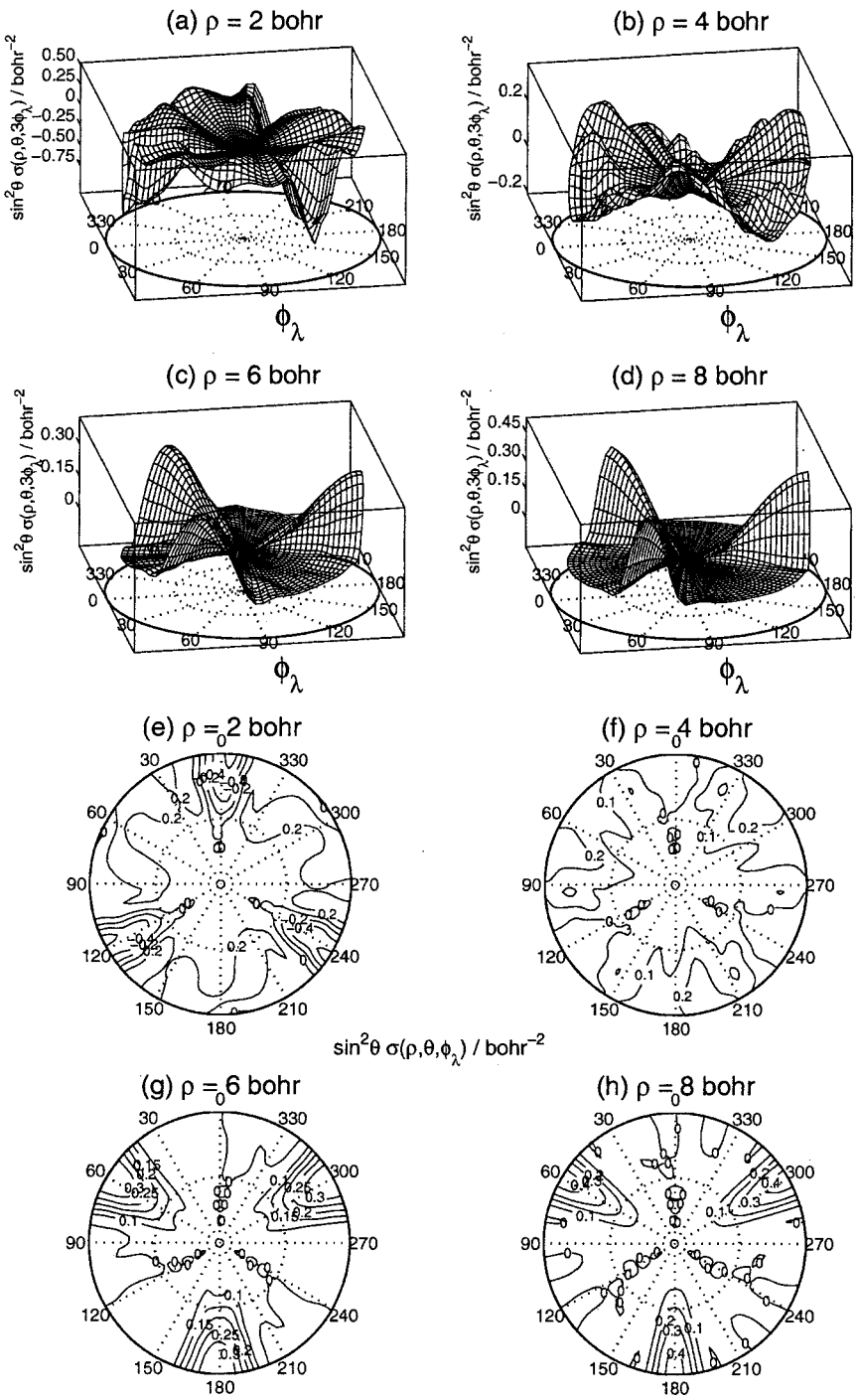

FIG. 3. The quantity $\sin^2\theta\,\sigma(\rho,\theta,3\phi_\lambda)$, in units of bohr^{-2}, with σ defined by Eq. (30), for the H_3 system as a function of θ and ϕ_λ, at (a) $\rho=2$ bohr, (b) $\rho=4$ bohr, (c) $\rho=6$ bohr, and (d) $\rho=8$ bohr. The circles on the bottom face of each of the panels are constant θ circles, with the solid circle corresponding to $\theta=90°$, and radial lines are constant ϕ_λ lines whose values are displayed on the periphery of the solid circle. Equatorial views of $\sin^2\theta\,\sigma(\rho,\theta,3\phi_\lambda)$ contours at (e) $\rho=2$ bohr, (f) $\rho=4$ bohr, (g) $\rho=6$ bohr, and (h) $\rho=8$ bohr. See the first paragraph of Sec. III A for the definition of the equatorial view.

corresponding $\langle w_{\mathrm{tra}}^{(1)\mathrm{ad}}\rangle_i$ from the minimum value $\langle w_{\mathrm{tra}}^{(1)\mathrm{ad}}\rangle_0$. These quantities will permit an assessment of the magnitude of the minimization achieved in the latter and of the relative importance of using Neumann boundary conditions on S_4, S_5, and S_6.

In the next section, we present the results obtained for the diabatization angle as well as those for the longitudinal and transverse parts of the first-derivative coupling vector. We will also discuss the magnitude of the transverse part in the dynamically relevant regions of nuclear configuration space, the importance of the Neumann boundary conditions used in its determination, and its possible effect on scattering calculations upon its reintroduction as a perturbation.

III. RESULTS AND DISCUSSION

A. Diabatization angle

The function $\sigma(\rho,\theta,3\phi_\lambda)$, needed to solve the Poisson equation, is displayed in Fig. 3, with a multiplicative factor of $\sin^2\theta$, as a function of θ and ϕ_λ for $\rho=2$, 4, 6, and 8 bohr. This factor is used to cancel out the pole behavior of σ associated with its $1/\sin^2\theta$ dependence. This source term also displays the permutation symmetry of the H_3 system. For $\rho=2$ bohr [panel (a)], it ($\sin^2\theta\,\sigma$) has sharp minima of about $0.75\,\mathrm{bohr}^{-2}$ at $\phi_\lambda=0°$, 120°, and 240° while displaying small oscillations around a flat value in other regions. For $\rho=8$ bohr [panel (d)], it displays sharp maxima of about

$0.45\,\text{bohr}^{-2}$ at $\phi_\lambda = 60°$, 180°, and 300° while staying flat with no oscillations in other regions. Both these extrema (sharp minima for $\rho = 2$ bohr and sharp maxima for $\rho = 8$ bohr) occur for all values of θ with the most pronounced behavior occurring at $\theta = 90°$ (collinear configurations). Its characteristics at $\rho = 4$ bohr [panel (b)] are midway between those at $\rho = 2$ bohr and $\rho = 8$ bohr, with no sharp features. Besides, at this hyperradius it has oscillations which show minima around $\phi_\lambda = 0°$, 120°, and 240° and maxima around $\phi_\lambda = 60°$, 180°, and 300°. At $\rho = 6$ bohr [panel (c)], its behavior is similar to that at $\rho = 8$ bohr. In panels (e)–(h) we depict equatorial views of $\sin^2\theta\,\sigma(\rho,\theta,3\phi_\lambda)$ contours and their mapping onto the $\overline{x}_\lambda\overline{y}_\lambda$ tangent plane of Fig. 1. This mapping is called the equatorial view because it corresponds to a non-perpendicular arc-length-preserving projection of the constant hyperradius hemisphere on a plane tangent to it at the point on its equator, defined by $\omega_\lambda = \gamma_\lambda = \pi/2$. This permits the viewing of all three possible atom–diatom arrangement channel regions (for the triatomic reaction) as well as the regions for which the three atoms are at comparable distances from each other, for a fixed hyperradius ρ. Maps of this kind have been used before.[18,52,62,63] This view of $\sin^2\theta\,\sigma(\rho,\theta,3\phi_\lambda)$ contours confirms the sharp minima behavior for $\rho = 2$ bohr and sharp maxima behavior for $\rho = 8$ bohr in different regions of the ϕ_λ space. They also confirm the flat regions of $0\,\text{bohr}^{-2}$ for $\rho = 6$ bohr and $\rho = 8$ bohr around $\phi_\lambda = 0°$, 120°, and 240° regions of configuration space. Analysis of $\mathbf{w}^{(1)\text{ad}}$ at these hyperradii (using their plots from Ref. 18) shows that in and around these regions of configuration space the coupling vector is about two orders of magnitude smaller than in the regions of space around $\phi_\lambda = 60°$, 180°, and 300°. This is also evident in the corresponding plots of $\mathbf{w}_{\text{lon}}^{(1)\text{ad}}$ (Fig. 9) and $\mathbf{w}_{\text{tra}}^{(1)\text{ad}}$ (Fig. 10) discussed in Sec. III D, since their sum gives the total coupling vector $\mathbf{w}^{(1)\text{ad}}$. In the three ϕ_λ regions mentioned above, the dominant $\mathbf{w}_{\text{lon}}^{(1)\text{ad}}$ is much smaller than in other regions. This negligibly small magnitude of the coupling vector leads to its negligible divergence as indicated by the source term $\sigma(\rho,\theta,3\phi_\lambda)$ plotted in panels (c), (d), (g), and (h) of Fig. 3.

Solution of the Poisson Eq. (40), subject to the boundary conditions of Eq. (42) and Eqs. (44)–(51) and the source term discussed above, furnishes $\gamma(\rho,\theta,3\phi_\lambda)$ in the domain of internal nuclear configuration space defined by Eq. (41), which is the entire ρ and θ space but one-sixth of the full ϕ_λ space. This can be extended to the full $0 \leqslant \phi_\lambda < 2\pi$ space by symmetry considerations. The diabatization angle $\beta(\rho,\theta,\phi_\lambda)$ is then obtained over the full domain U by using $\gamma(\rho,\theta,3\phi_\lambda)$ together with Eq. (35).

Figure 4 [panels (a)–(d)] depicts the diabatization angle $\beta(\rho,\theta,\phi_\lambda)$ as a function of θ and ϕ_λ for four different hyperradii. Panels (a), (b), (c), and (d) correspond to the fixed hyperradii of 2 bohr (tight geometries), 4 bohr, 6 bohr, and 8 bohr (asymptotic geometries), respectively. Panels (e)–(h) display the equatorial views of β contours corresponding to panels (a)–(d) through their mapping onto the $\overline{x}_\lambda\overline{y}_\lambda$ tangent plane of Fig. 1. Since near conical-intersection geometries, and even at other geometries, $\beta(\rho,\theta,\phi_\lambda)$ is dominated by the $\phi_\lambda/2$ term, we plot in Fig. 5 [panels (a)–(d)] $\gamma(\rho,\theta,3\phi_\lambda)$ as a function of θ and ϕ_λ for the same hyperradii as before and the corresponding equatorial views in panels (e)–(h), respectively. In each of the panels in Figs. 4 and 5, the hyperradius ρ is kept fixed and the hyperangle ϕ_λ is varied from 0 to 2π along the circle shown at the bottom. In addition, the hyperangle θ is varied from 0 to $\pi/2$, from the center of that circle (corresponding to $\theta = 0$ or conical intersection geometries) to its edge (corresponding to $\theta = \pi/2$ or collinear geometries).

Panels (a)–(d) of Fig. 6 display cuts of the $\gamma(\rho,\theta,3\phi_\lambda)$ plots shown in panels (a)–(d), respectively, of Fig. 5 at three values of θ (5°, 45°, and 90°) for the same four values of ρ. The corresponding DMBE angle, $\gamma^{\text{DMBE}}(\rho,\theta,3\phi_\lambda)$, is displayed in panels (e)–(h) of Fig. 6 for the same θ cuts and hyperradii. Since $\gamma^{\text{DMBE}}(\rho,\theta,3\phi_\lambda)$ is accurate in the vicinity of the conical intersection, a quantity Δ_γ is defined as the maximum difference between γ and γ^{DMBE} over all values of ϕ_λ, keeping the values of ρ and θ fixed:

$$\Delta_\gamma(\rho,\theta) = \max[\,\gamma(\rho,\theta,3\phi_\lambda) - \gamma^{\text{DMBE}}(\rho,\theta,3\phi_\lambda)\,]_{\phi_\lambda}. \tag{56}$$

In Fig. 7, Δ_γ is depicted as a function of θ for the same four values of the hyperradius ρ, since it provides an indication of the ρ-dependent difference between γ^{DMBE} and γ as a function of θ. As the latter increases from 0° to 90°, the corresponding configuration moves away from the conical intersection. Figure 8 depicts $\gamma_{6\text{D}}$ obtained from the 6 Dirichlet boundary conditions calculation $\mathbf{b}_2$ described in Sec. II D. Figures 4–8 are further discussed in Sec. III D.

B. Longitudinal and transverse parts of the first-derivative coupling vector

The gradient of $\beta(\rho,\theta,\phi_\lambda)$ furnishes $\mathbf{w}_{\text{lon}}^{(1)\text{ad}}(\mathbf{q})$, and Eq. (28) then gives $\mathbf{w}_{\text{tra}}^{(1)\text{ad}}(\mathbf{q})$. We have previously calculated the components of $\mathbf{w}^{(1)\text{ad}}(\mathbf{q})$ in the directions of the hyperspherical unit vectors associated with ρ, θ, and ϕ_λ.[18] We can now calculate the corresponding components of $\mathbf{w}_{\text{lon}}^{(1)\text{ad}}$ and $\mathbf{w}_{\text{tra}}^{(1)\text{ad}}$. The corresponding $\mathcal{Q}$ space Cartesian components of $\mathbf{w}_{\text{lon}}^{(1)\text{ad}}$ are given by

$$\begin{pmatrix} w_{\text{lon},x}^{(1)\text{ad}} \\ w_{\text{lon},y}^{(1)\text{ad}} \\ w_{\text{lon},z}^{(1)\text{ad}} \end{pmatrix} = \begin{pmatrix} \sin\theta\cos\phi_\lambda & \cos\theta\cos\phi_\lambda & -\sin\phi_\lambda \\ \sin\theta\sin\phi_\lambda & \cos\theta\sin\phi_\lambda & \cos\phi_\lambda \\ \cos\theta & -\sin\theta & 0 \end{pmatrix} \times \begin{pmatrix} w_{\text{lon},\rho}^{(1)\text{ad}} \\ w_{\text{lon},\theta}^{(1)\text{ad}} \\ w_{\text{lon},\phi_\lambda}^{(1)\text{ad}} \end{pmatrix} \tag{57}$$

and those of $\mathbf{w}_{\text{tra}}^{(1)\text{ad}}$ by an analogous expression.

In Fig. 9, we present perspective plots of the longitudinal part of first-derivative coupling vector $[\mathbf{w}_{\text{lon}}^{(1)\text{ad}}]$ as a function of the hyperangle ϕ_λ, at a fixed hyperradius ρ (4 bohr, 6 bohr, and 8 bohr) and a fixed hyperangle θ. In Cartesian language, this is equivalent to varying x and y on a circle and keeping z fixed. The corresponding adiabatic ground state and first-excited state electronic energies are displayed in Figs. 5–7 of Ref. 18. Figure 10 presents the corresponding perspective plots of the transverse part $[\mathbf{w}_{\text{tra}}^{(1)\text{ad}}]$ of the first-derivative coupling vector. In both Figs. 9 and 10, panel (a) corresponds to $\theta = 1°$ (a value very close to the conical intersection geometries of $\theta = 0°$), panel (b) to $\theta = 30°$, panel

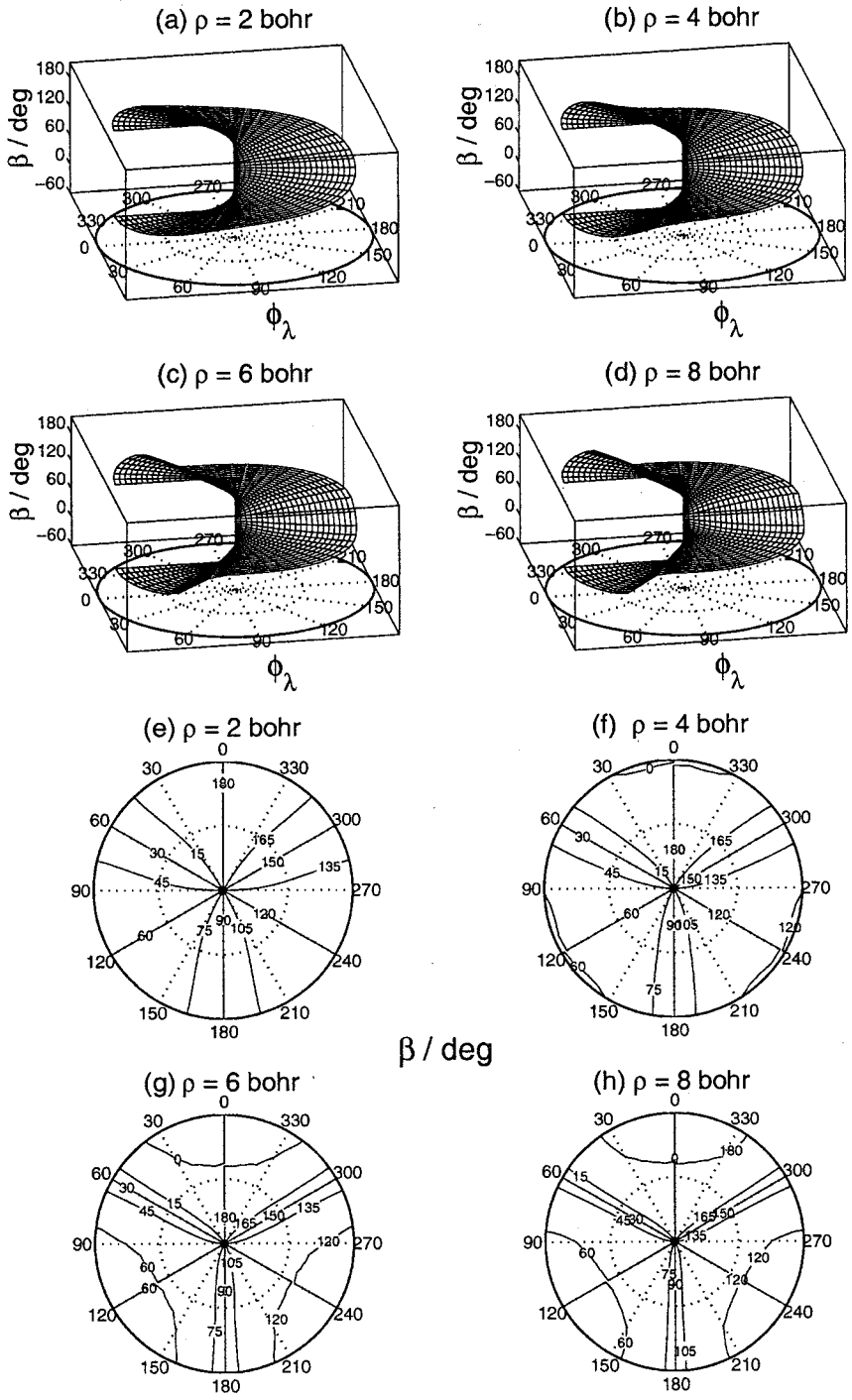

FIG. 4. The diabatization angle $\beta(\rho,\theta,\phi_\lambda)$, in degrees, for the H_3 system at (a) $\rho=2$ bohr, (b) $\rho=4$ bohr, (c) $\rho=6$ bohr, and (d) $\rho=8$ bohr. The bottom face of the panels are similar to those of the corresponding panels of Fig. 3. The equatorial view of β contours is also given at (e) $\rho=2$ bohr, (f) $\rho=4$ bohr, (g) $\rho=6$ bohr, and (h) $\rho=8$ bohr.

(c) to $\theta=60°$, and the panel (d) to $\theta=90°$ (collinear geometries). The origin of the coupling vectors lies on a circle that corresponds to a fixed θ on the hyperspherical coordinate hemisphere for the indicated value of ρ. This circle maps the full ϕ_λ range of 0° to 360°. The coupling vectors shown in these two figures correspond to the hyperspherical space being mapped by this circle. Above each of the panels two scales are given. The one in units of bohr corresponds to the internal nuclear configuration space corresponding to the full 0° to 360° ϕ_λ range spanned on the xy plane. The second one, in units of bohr^{-1}, corresponds to the three-dimensional space sampled by the x, y, and z components of the coupling vector. The two spaces coexist on the xy plane.

The $\mathbf{w}_{\text{lon}}^{(1)\text{ad}}$ and $\mathbf{w}_{\text{tra}}^{(1)\text{ad}}$ plots at $\theta=1°$ [panel (a) in Figs. 9 and 10] have been included to show their behavior near the conical intersection. The $\theta=90°$ case [panel (d) in these two figures], corresponds to collinear geometries for the triatomic system. This case is important for lower energies due to the collinear dominance of the $H+H_2$ reaction at those energies, as will be discussed in Sec. III D. The $\theta=30°$ and $\theta=60°$ cases [panels (b) and (c), respectively] have been included to gauge the importance of the coupling vector away from the conical intersection as well as from the collinear geometries. Figure 11 displays the corresponding perpective plots of the $\mathbf{w}_{\text{tra,6D}}^{(1)\text{ad}}$ vector, obtained in the $\mathbf{b}_2$ calculation described in Sec.

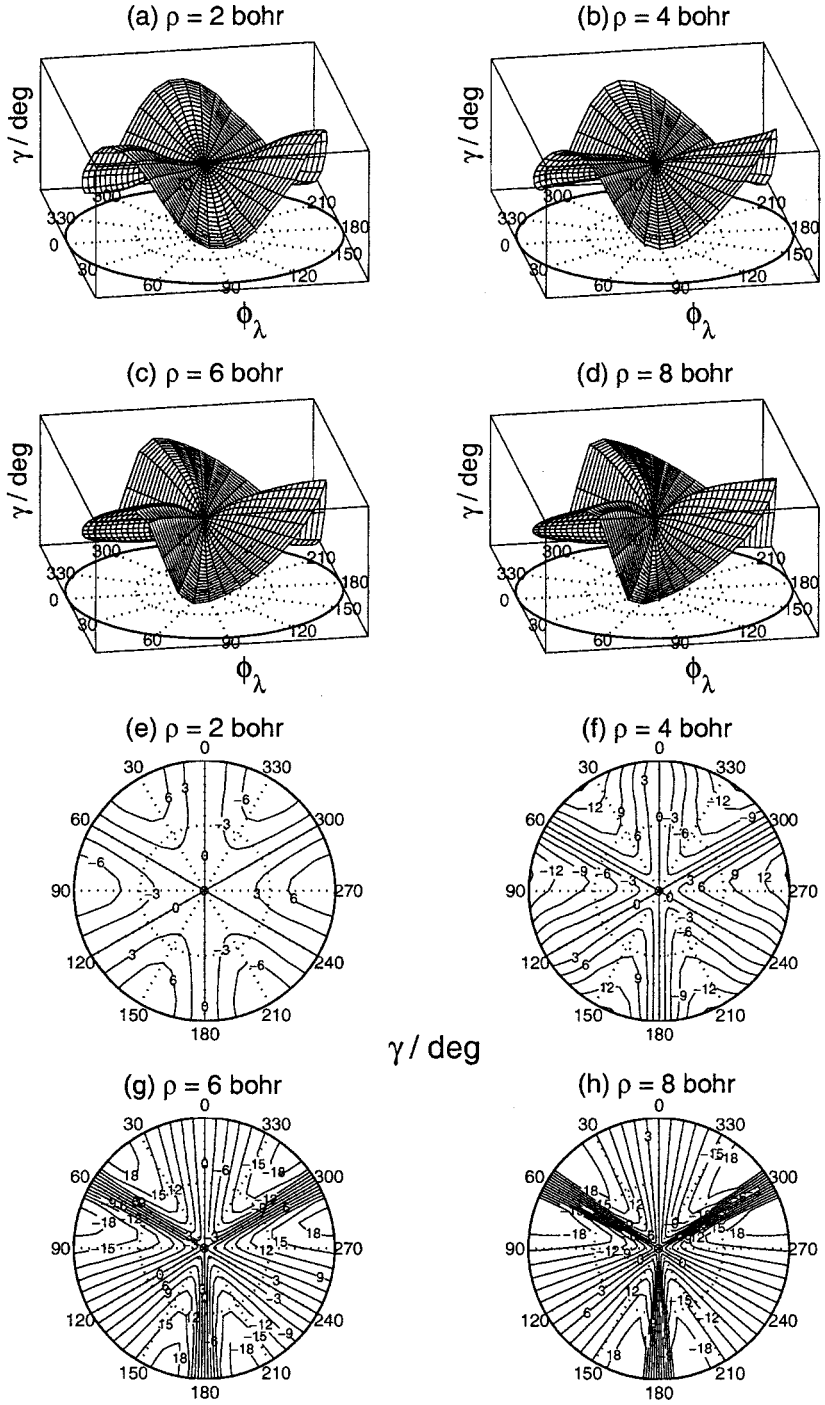

FIG. 5. Same as Fig. 4 for the $\gamma(\rho,\theta,3\phi_\lambda)$ part of the diabatization angle $\beta(\rho,\theta,\phi_\lambda)$ defined by Eq. (35).

II D using 6 Dirichlet boundary conditions, at $\rho=4$, 6, and 8 bohr. It has been provided to permit a comparison of the magnitude of this vector with that obtained from the optimal calculation (shown in Fig. 10).

We can now check whether the $\mathbf{w}_{\text{lon}}^{(1)\text{ad}}$ and $\mathbf{w}_{\text{tra}}^{(1)\text{ad}}$ described above satisfy Eqs. (25) and (26), which are consequences of the geometric phase theorem. This is a numerical self-consistency check. Writing Eq. (25) explicitly in terms of $\mathbf{w}_{\text{lon}}^{(1)\text{ad}}$ and the symmetrized hyperspherical coordinates, and taking for path $\mathcal{L}$ a closed loop around the conical intersection between the $1\,^2A'$ and $2\,^2A'$ states of H_3, we get for the longitudinal topological phases [Eq. (23)] the expression

$$\Phi_{\text{T,lon}}(\rho,\theta)=\oint \mathrm{w}_{\text{lon},\phi_\lambda}^{(1)\text{ad}}(\rho,\theta,\phi'_\lambda)\rho\sin\theta\,d\phi'_\lambda, \tag{58}$$

where $\mathrm{w}_{\text{lon},\phi_\lambda}^{(1)\text{ad}}$ is the ϕ_λ-component of the $\mathbf{w}_{\text{lon}}^{(1)\text{ad}}$ vector. Similarly, the transverse topological phase [Eq. (24)], can be written in terms of $\mathbf{w}_{\text{tra}}^{(1)\text{ad}}$ as

$$\Phi_{\text{T,tra}}(\rho,\theta)=\oint \mathrm{w}_{\text{tra},\phi_\lambda}^{(1)\text{ad}}(\rho,\theta,\phi'_\lambda)\rho\sin\theta\,d\phi'_\lambda, \tag{59}$$

where $\mathrm{w}_{\text{tra},\phi_\lambda}^{(1)\text{ad}}$ is the ϕ_λ-component of the $\mathbf{w}_{\text{tra}}^{(1)\text{ad}}$ vector. The

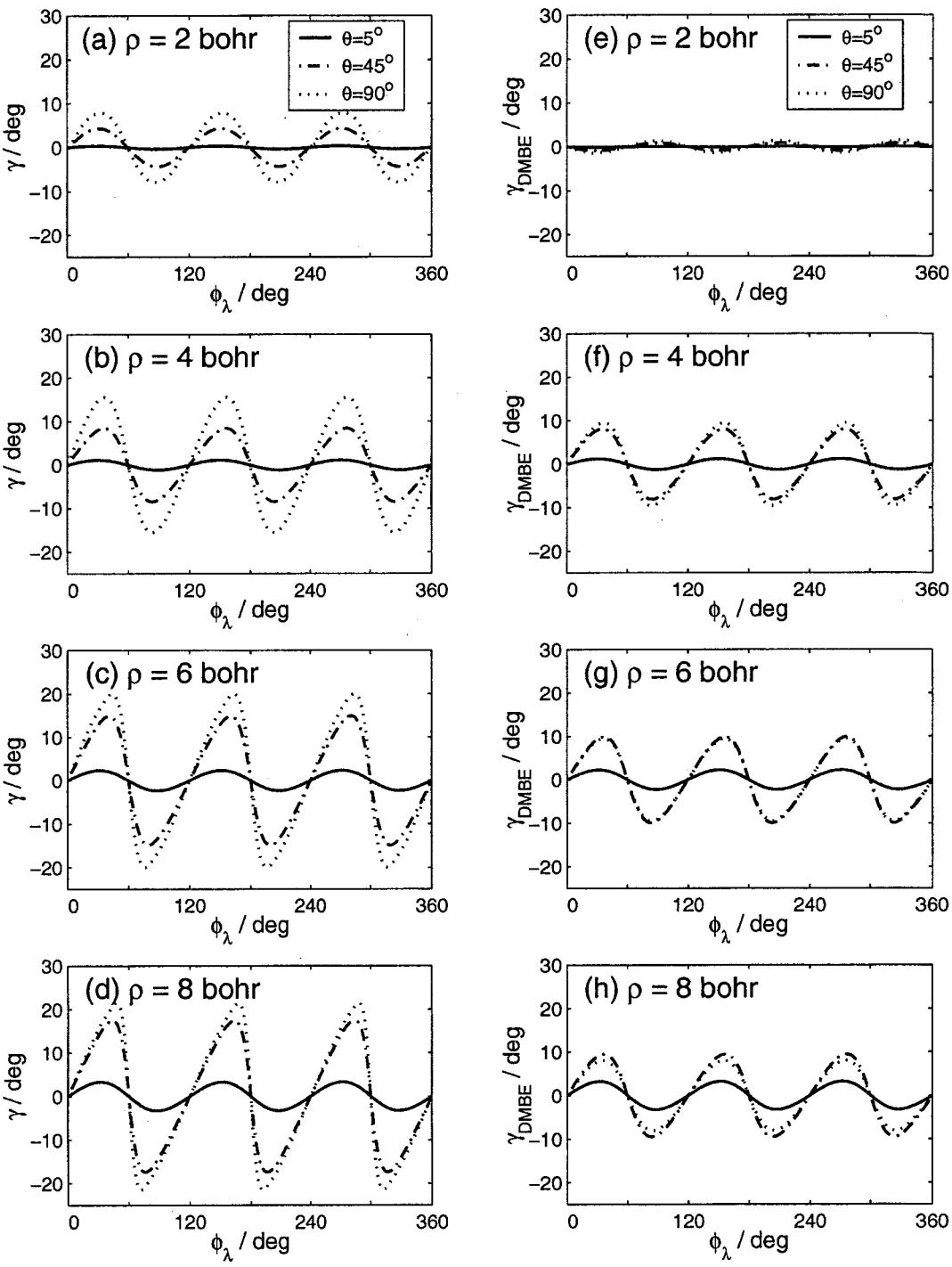

FIG. 6. Cuts of $\gamma(\rho,\theta,3\phi_\lambda)$ (shown in Fig. 5) at three values of θ: 5° (solid line), 45° (dashed–dotted line), and 90° (dotted line) for (a) $\rho=2$ bohr, (b) $\rho=4$ bohr, (c) $\rho=6$ bohr, and (d) $\rho=8$ bohr and the corresponding cuts of $\gamma^{\mathrm{DMBE}}(\rho,\theta,3\phi_\lambda)$ at the same three values of θ, for (e) $\rho=2$ bohr, (f) $\rho=4$ bohr, (g) $\rho=6$ bohr, and (h) $\rho=8$ bohr.

corresponding longitudinal and transverse open-path phases associated with Eq. (21) can be expressed in the symmetrized hyperspherical coordinates as

$$\Phi_{\mathrm{lon}}(\phi_\lambda;\rho,\theta)=\int_0^{\phi_\lambda} w^{(1)\mathrm{ad}}_{\mathrm{lon},\phi_\lambda}(\rho,\theta,\phi'_\lambda)\rho\sin\theta\,d\phi'_\lambda \qquad (60)$$

and

$$\Phi_{\mathrm{tra}}(\phi_\lambda;\rho,\theta)=\int_0^{\phi_\lambda} w^{(1)\mathrm{ad}}_{\mathrm{tra},\phi_\lambda}(\rho,\theta,\phi'_\lambda)\rho\sin\theta\,d\phi'_\lambda$$
$$=\int_0^{\phi_\lambda} w^{(1)\mathrm{ad}}_{\phi_\lambda}(\rho,\theta,\phi'_\lambda)\rho\sin\theta\,d\phi'_\lambda-\pi, \qquad (61)$$

where $p=1$ is used along with Eq. (26), since $\mathcal{L}$ encircles the

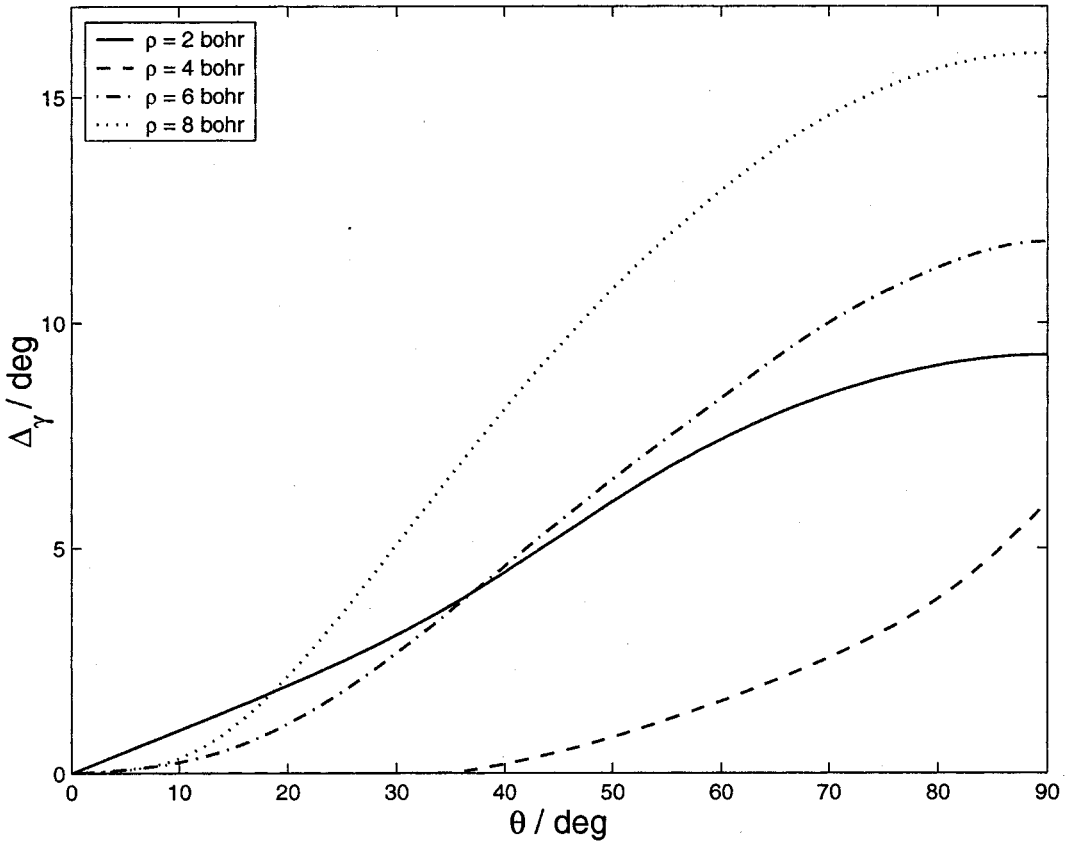

FIG. 7. Plots of Δ_γ, defined by Eq. (56), as a function of θ for four values of ρ: 2 bohr (solid line), 4 bohr (dashed line), 6 bohr (dashed–dotted line), and 8 bohr (dotted line).

one conical intersection mentioned above. The relation between these open-path phases and the corresponding topological phases is obviously

$$\Phi_{\mathrm{T,lon}}(\rho,\theta)=\Phi_{\mathrm{lon}}(2\pi;\rho,\theta), \tag{62}$$

$$\Phi_{\mathrm{T,tra}}(\rho,\theta)=\Phi_{\mathrm{tra}}(2\pi;\rho,\theta). \tag{63}$$

In Fig. 12 [panels (a)–(d)], we display $\Phi_{\mathrm{lon}}(\phi_\lambda;\rho,\theta)$ as a function of ϕ_λ evaluated using Eq. (60) for four values of ρ (2 bohr through 8 bohr every 2 bohr, respectively) and four values of θ (1°, 30°, 60°, and 90°). In Fig. 12 [panels (e)–(h)] we depict $\Phi_{\mathrm{tra}}(\phi_\lambda;\rho,\theta)$ as a function of ϕ_λ evaluated using Eq. (61) at the same values of ρ and θ. The values of the corresponding topological phases $\Phi_{\mathrm{T,lon}}(\rho,\theta)$ and $\Phi_{\mathrm{T,tra}}(\rho,\theta)$ can be read off these panels by taking the open-path phases at $\phi_\lambda=2\pi$ (or 360°). The results shown in Figs. 9–12 are analyzed in Sec. III D.

C. Diabatic potential energy surfaces

Once the diabatization angle $\beta(\mathbf{q})$ is known from the solution of Poisson equation, the diabatic energy matrix $\boldsymbol{\varepsilon}^d(\mathbf{q})$ can be evaluated using Eq. (20) which in extended form is

$$\begin{aligned}\boldsymbol{\varepsilon}^d(\mathbf{q})&=\begin{pmatrix}\varepsilon^d_{11}(\mathbf{q}) & \varepsilon^d_{12}(\mathbf{q})\\ \varepsilon^d_{21}(\mathbf{q}) & \varepsilon^d_{22}(\mathbf{q})\end{pmatrix}\\ &=\tilde{\mathbf{U}}[\beta(\mathbf{q})]\begin{pmatrix}\varepsilon^{\mathrm{ad}}_1(\mathbf{q}) & 0\\ 0 & \varepsilon^{\mathrm{ad}}_2(\mathbf{q})\end{pmatrix}\mathbf{U}[\beta(\mathbf{q})],\end{aligned} \tag{64}$$

where $\mathbf{U}[\beta(\mathbf{q})]$ is given by Eq. (16). $\varepsilon^{\mathrm{ad}}_1(\mathbf{q})$ and $\varepsilon^{\mathrm{ad}}_2(\mathbf{q})$ are, respectively the adiabatic ground and first-excited PESs which have been fitted earlier to the *ab intio* energies using the DMBE-single-polynomial (DSP) method.[18] From this expression we get

$$\begin{aligned}\varepsilon^d_{11}(\mathbf{q})&=\cos^2\beta(\mathbf{q})\varepsilon^{\mathrm{ad}}_1(\mathbf{q})+\sin^2\beta(\mathbf{q})\varepsilon^{\mathrm{ad}}_2(\mathbf{q}),\\ \varepsilon^d_{22}(\mathbf{q})&=\sin^2\beta(\mathbf{q})\varepsilon^{\mathrm{ad}}_1(\mathbf{q})+\cos^2\beta(\mathbf{q})\varepsilon^{\mathrm{ad}}_2(\mathbf{q}),\\ \varepsilon^d_{12}(\mathbf{q})&=\varepsilon^d_{21}(\mathbf{q})=\cos\beta(\mathbf{q})\sin\beta(\mathbf{q})\ \ [\varepsilon^{\mathrm{ad}}_2(\mathbf{q})-\varepsilon^{\mathrm{ad}}_1(\mathbf{q})].\end{aligned} \tag{65}$$

Panels (a) and (b) of Figs. 13 and 14, and Fig. 15 show the adiabatic and diabatic PES contours in the $X_\lambda Z_\lambda$ plane of Fig. 1, which corresponds to the $\gamma_\lambda=0°$ and 180° cuts. Panels (c) and (d) in Figs. 13 and 14 show these contours in the YZ_λ plane of Fig. 1, which corresponds to the $\gamma_\lambda=90°$ cut. Figure 16 depicts the conical intersection energies, corresponding to equilateral triangle configurations, as a function of ρ for four sets of electronically adiabatic *ab initio* PES calculations: DSP,[18] LSTH,[64–66] DMBE,[47] and EQMC.[63] The DSP curve corresponds to the $Z_\lambda=0$ energies in panels (c)

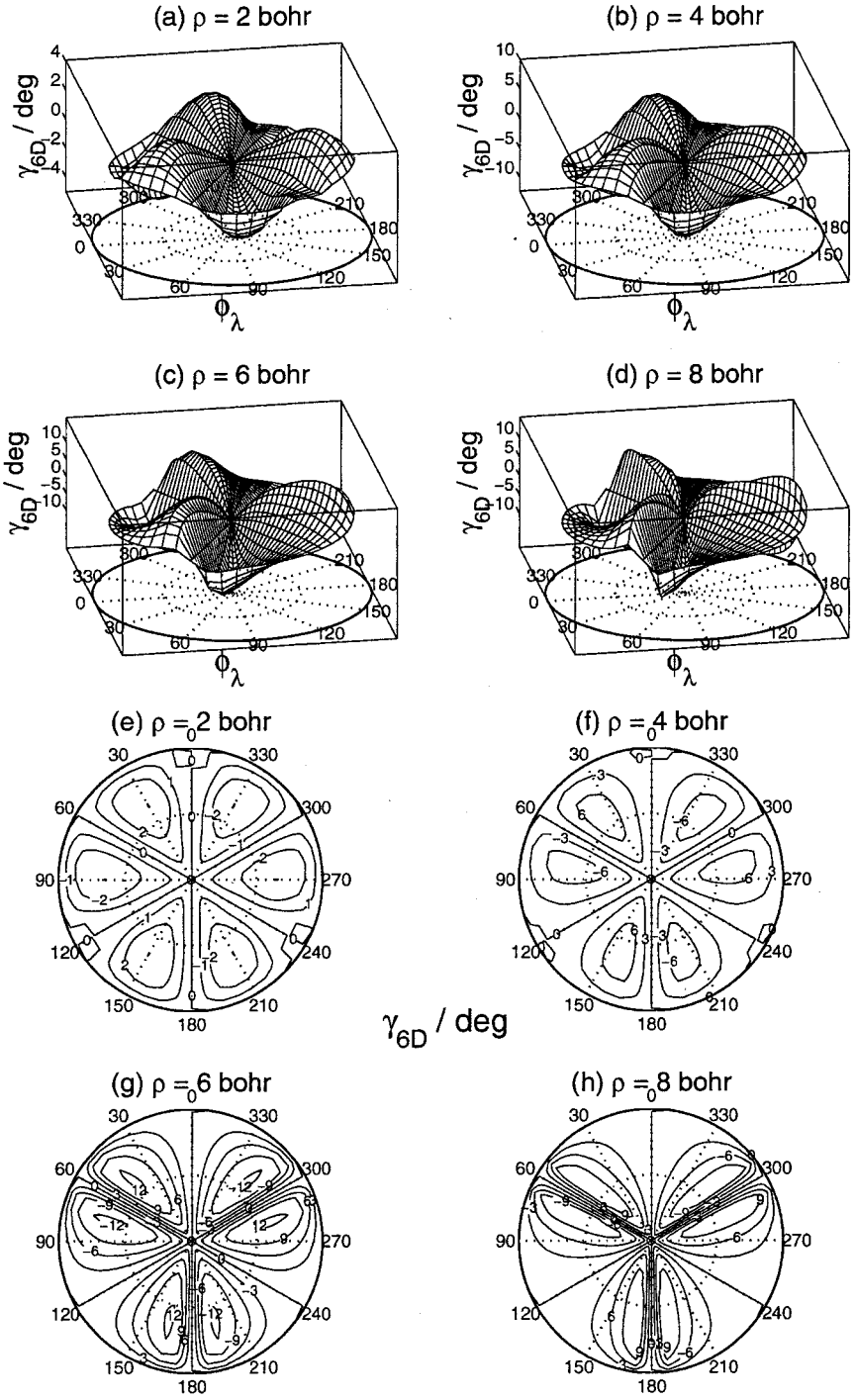

FIG. 8. Plots of γ_{6D}, the γ angle obtained from the solution of a Poisson equation using Dirichlet boundary conditions at all six boundaries. Panels (a)–(d) show the three-dimensional plots and panels (e)–(h) show the equatorial view of its contours similar to Fig. 4.

and (d) of Fig. 13. Figures 17–19 show equatorial views (described in the first paragraph of Sec. III A) of the PES contours through their mapping onto the $\overline{x_\lambda y_\lambda}$ tangent plane of Fig. 1. In the next section we will discuss the features of the adiabatic and diabatic PESs through their contours displayed in Figs. 13–15 and 17–19.

D. Discussion

Figure 4 [panels (a)–(d)] displays the diabatization angle $\beta(\rho,\theta,\phi_\lambda)$ for four fixed values of the hyperradius ρ. In all these panels, the dominance of the $\phi_\lambda/2$ part of β is clearly visible: As ϕ_λ increases from 0 to 2π, β varies from a value close to 0 to a value close to π. Besides this behavior, some small variations are visible in the ϕ_λ-dependence of β. Due to the dominance of the $\phi_\lambda/2$ term, it is hard to distinguish the β at $\rho=2$ bohr (corresponding to a compact set of geometries) from that at $\rho=8$ bohr (corresponding to a near-asymptotic set of geometries), except for the small variations mentioned above which become slightly more prominent as ρ increases from 2 bohr to 8 bohr.

Panels (e)–(h) of Fig. 4 depict the equatorial view of the contours corresponding to the β panels (a)–(d). In these equatorial views, the three atom–diatom arrangement channels lie along the $\phi_\lambda=0°$, 120°, and 240° lines. These pan-

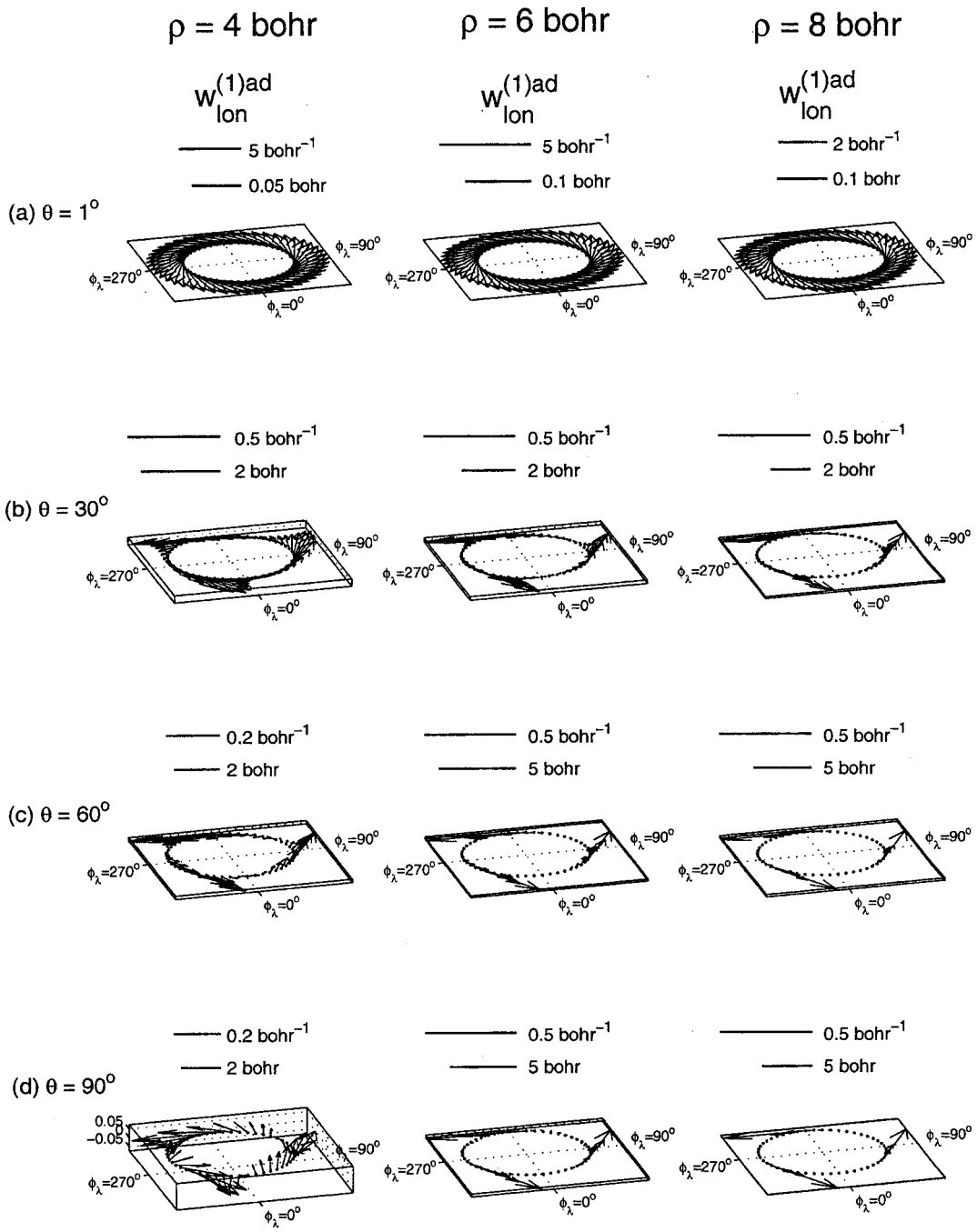

FIG. 9. Longitudinal (removable) part of the *ab initio* first-derivative coupling vector, $\mathbf{w}_{lon}^{(1)ad}(\rho,\theta,\phi_\lambda)$ as a function of ϕ_λ for $\rho=4$ bohr, 6 bohr, and 8 bohr and (a) $\theta=1°$ (near-conical intersection geometries), (b) $\theta=30°$, (c) $\theta=60°$, and (d) $\theta=90°$ (collinear geometries).

els show that their contour lines are mainly radial, independently of the value of ρ. This is a consequence of having set $\gamma=0°$ at $\phi_\lambda=0°$ and 60° (the S_1 and S_2 boundary surfaces), for the reasons given in Sec. II D. They also show clearly the $\phi_\lambda/2$ dependence of β with the contour values increasing with an increase in ϕ_λ. Hence, although in this view the β contours seem to have P_3 symmetry they actually don't, due to this $\phi_\lambda/2$ dependence. The feature that is clear in these contours of β that was not very obvious in panels (a)–(d) of Fig. 4 is that β increases sharply with an increase in ϕ_λ around the $\phi_\lambda=60°$, 180°, and 300° lines and increases slowly in other regions. This sharp increase becomes sharper with an increase in ρ as we go from panel (e) ($\rho=2$ bohr) to panel (h) ($\rho=8$ bohr). In each panel, the line corresponding to $\phi_\lambda=0°$ and 180° is interesting because on the $\phi_\lambda=0°$ line β is zero and on the 180° line it is 90°. This has the following effect on the behavior of diabatic surfaces ε_{11}^d, ε_{22}^d, and ε_{12}^d [using Eqs. (65) discussed in Sec. III C] and on the diabatic nuclear wave functions χ_1^d and χ_2^d [using Eqs. (18) and (16) discussed in the introduction]: (a) the coupling PES ε_{12}^d is zero on both these ϕ_λ lines; (b) on the $\phi_\lambda=0°$ line, $\varepsilon_{11}^d=\varepsilon_1^{ad}$ and $\varepsilon_{22}^d=\varepsilon_2^{ad}$, which means that the adiabatic and diabatic nuclear wave functions coincide on

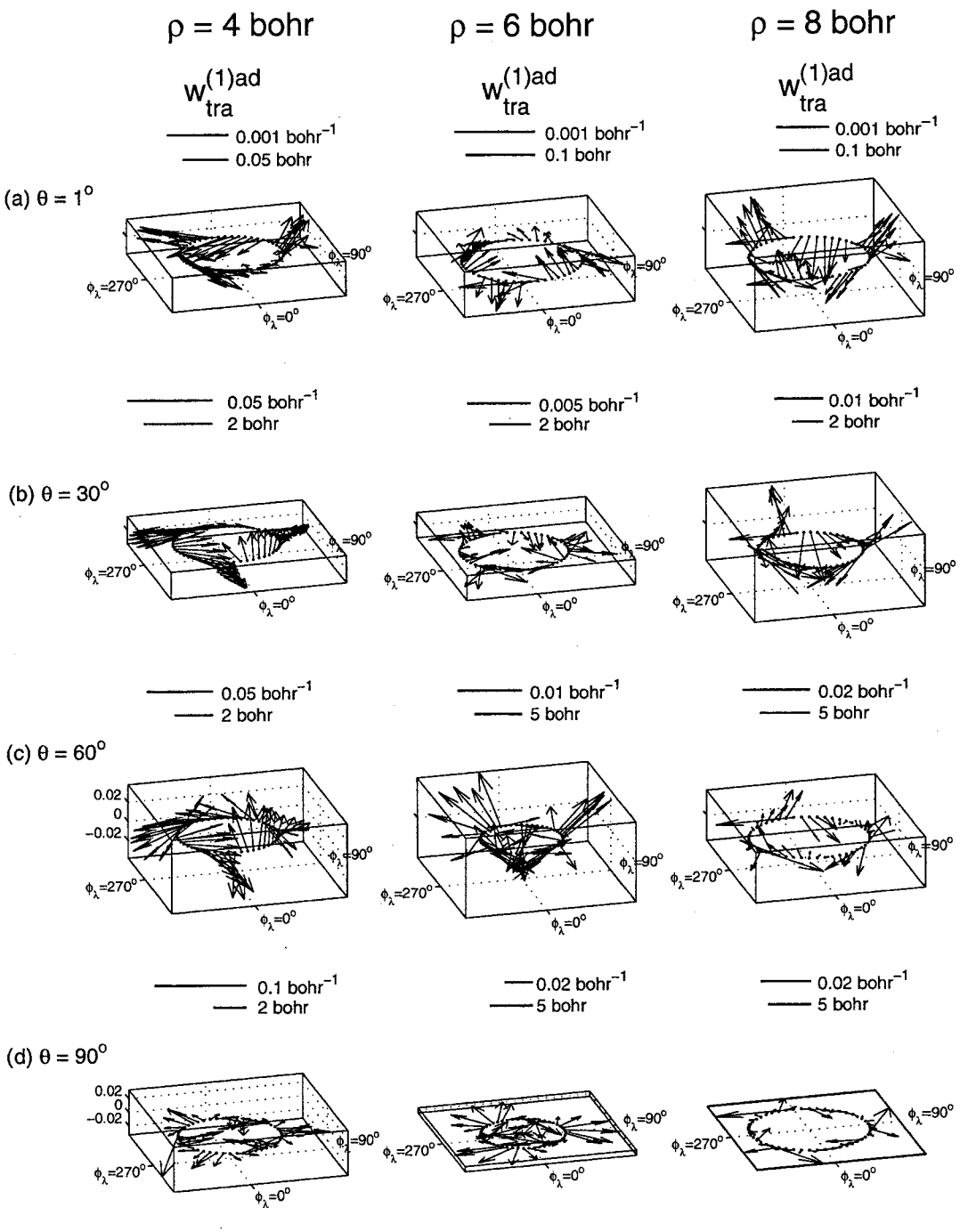

FIG. 10. Same as Fig. 9 for the transverse (nonremovable) part of the *ab initio* first-derivative coupling vector, $\mathbf{w}_{\mathrm{tra}}^{(1)\mathrm{ad}}(\rho,\theta,\phi_\lambda)$.

this line; and (c) on the $\phi_\lambda = 180°$ line, $\varepsilon_{11}^d = \varepsilon_2^{\mathrm{ad}}$ and $\varepsilon_{22}^d = \varepsilon_1^{\mathrm{ad}}$, which means that the adiabatic nuclear wave functions are switched in the diabatic representation on this line with one of them switching sign also, i.e., $\chi_1^d = \chi_2^{\mathrm{ad}}$ and $\chi_2^d = -\chi_1^{\mathrm{ad}}$. This provides good physical insight into the behavior of the diabatic PESs and diabatic nuclear wave functions in terms of their adiabatic counterparts on the $\phi_\lambda =$ constant half-planes in configuration space just considered. Other interesting ϕ_λ half-planes are those corresponding to 45° and 135° because along them ε_{11}^d and ε_{22}^d coincide.

It is hard to see any quantitative variation in β as a function of the hyperangle θ. To make this and previously mentioned distinctions clear, panels (a)–(d) of Fig. 5 display the $\gamma(\rho,\theta,3\phi_\lambda)$ part of the diabatization angle, which does not contain the dominant $\phi_\lambda/2$ term. In all these panels, the P_3 symmetry is visible, as γ repeats itself every $2\pi/3$ radians. For $\rho = 2$ bohr, γ fluctuates as a function of ϕ_λ between $-5°$ and $+5°$. As a function of θ (looking from the center of the bottom circle to its edge), it starts from 0° at $\theta = 0°$ and increases (or decreases) to its maximum (or minimum) value at $\theta = 90°$. For $\rho = 4$ bohr (which is an important region for the reaction dynamics), the oscillations of γ with ϕ_λ are sharper (as compared to the $\rho = 2$ bohr case), and have a larger amplitude, staying between $-16°$ and $+16°$. As θ is

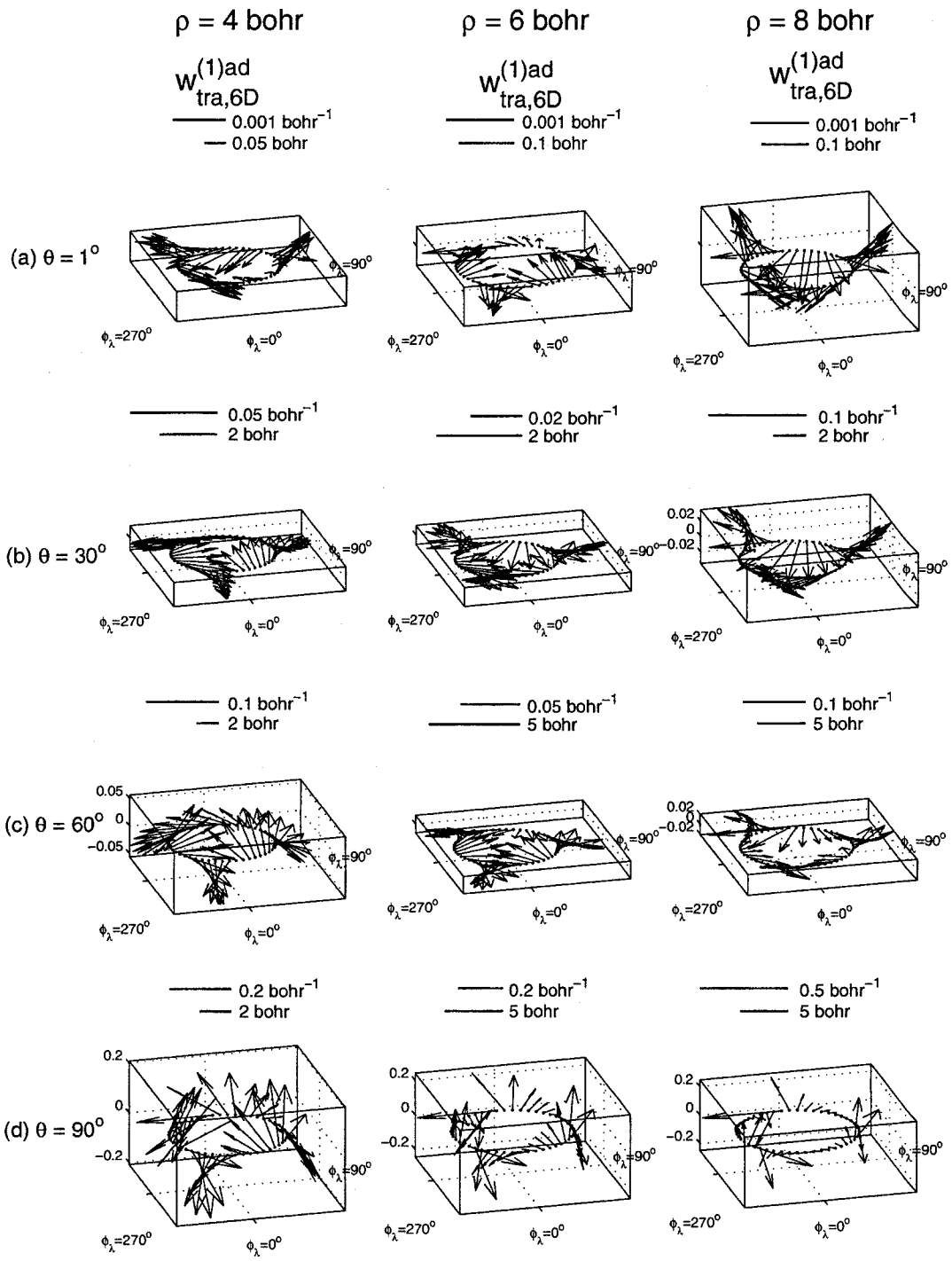

FIG. 11. Same as Fig. 9 for the transverse (nonremovable) part of the *ab initio* first-derivative coupling vector $\mathbf{w}^{(1)\mathrm{ad}}_{\mathrm{tra,6D}}(\rho,\theta,\phi_\lambda)$, obtained using the same Dirichlet boundary conditions as in Fig. 8.

varied, γ has the same behavior as that for the $\rho=2$ bohr case. For $\rho=6$ bohr and 8 bohr γ displays sharper oscillations, and amplitudes that stay between $-20°$ and $+20°$. This indicates that it is approaching its asymptotic limit as ρ increases. Their θ-dependence is similar to that for the $\rho=2$ bohr and 4 bohr cases. Since the diabatization matrix $\mathbf{U}[\beta(\mathbf{q})]$ elements are sines and cosines of β [see Eq. (16)], the dominance of the $\phi_\lambda/2$ term manifests itself as a change in the sign of the electronic and the nuclear adiabatic wave functions and forces the diabatic wave functions to be single valued, as discussed previously after Eq. (35). The γ term in that equation is important in determining the characteristics of the diabatic PESs that appear in Eq. (19).

Panels (e)–(h) of Fig. 5 depict equatorial views of γ contours corresponding to panels (a)–(d), respectively. These panels show the expected P_3 symmetry. Again, the contour lines have a strong radial behavior for all values of ρ due to the choice of boundary conditions on S_1 and S_2 just mentioned. In addition, the sharp rise observed in the β panels discussed earlier around the $\phi_\lambda=60°$, 180°, and 300° lines

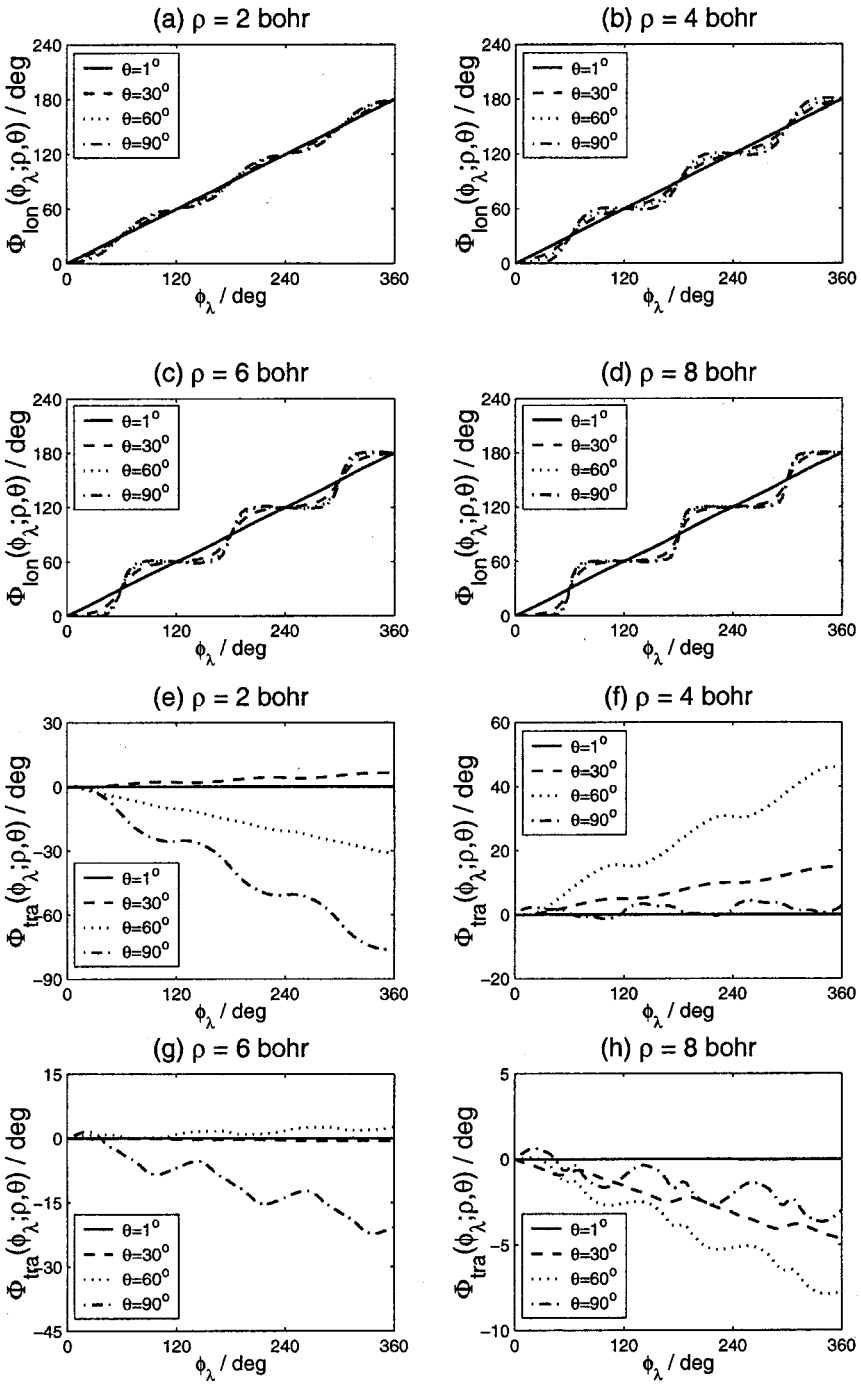

FIG. 12. Longitudinal $\Phi_{lon}(\phi_\lambda;\rho,\theta)$ and transverse $\Phi_{tra}(\phi_\lambda;\rho,\theta)$ open path phases as a function of ϕ_λ for four values of θ: 1° (solid line), 30° (dashed line), 60° (dotted line), and 90° (dashed–dotted line) for each of the four values of ρ: (a) and (e) 2 bohr, (b) and (f) 4 bohr, (c) and (g) 6 bohr, and (d) and (h) 8 bohr.

is manifested in these γ contours with the sharpness rising with an increase in ρ as we go from panel (e) ($\rho=2$ bohr) to panel (h) ($\rho=8$ bohr). Across these ϕ_λ lines γ goes from a large positive value to a large negative value, the absolute value of which also increases with ρ.

Three constant-θ cuts of γ plots in Fig. 5, which provide additional insight into the features of γ, are shown in Fig. 6 [panels (a)–(d)]. In each of these panels, the $\theta=5°$ cut (shown as a solid line) depicts the behavior of γ in the vicinity of equilateral triangle geometries. The $\theta=90°$ cut (dotted line) shows it for collinear geometries and the 45° cut (dashed–dotted line) shows it for a set of intermediate geometries. For all three cuts the amplitude of the oscillations in γ is smallest for $\rho=2$ bohr and increases as ρ increases to 8 bohr. The increase in this amplitude is largest in going from $\rho=2$ bohr to 4 bohr and tapers off by 8 bohr. Another interesting feature not very clear in the γ plots of Fig. 5 is that γ, which repeats itself every $2\pi/3$ radians with a maximum in the first half and a minimum in the second-half of any $2\pi/3$ radians period in ϕ_λ, does not display that maximum (or minimum) at the exact middle of those halves but is skewed towards the middle of those full $2\pi/3$ radians periods. The corresponding cuts for γ^{DMBE} are displayed in Fig. 6 [panels (e)–(h)] for comparison. For $\rho=2$ bohr,

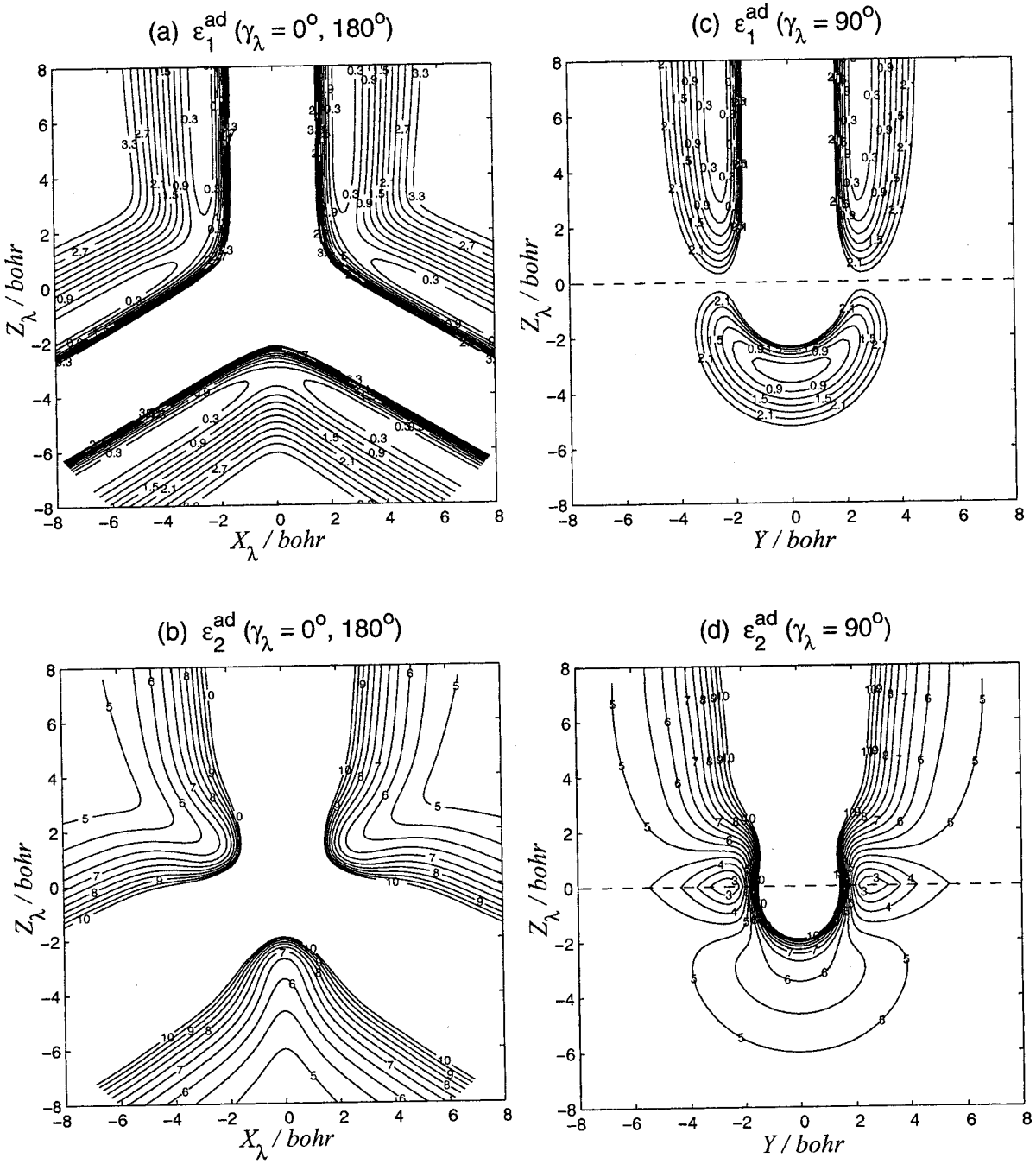

FIG. 13. (a) Adiabatic ground state (ε_1^{ad}) energy contours in the $X_\lambda Z_\lambda$ plane of Fig. 1 for a collinear approach ($\gamma_\lambda = 0°$ or 180°) of the H atom to the H_2 molecule; (b) corresponding contours for the first-excited state (ε_2^{ad}) energies; (c) ε_1^{ad} contours in the YZ_λ plane of Fig. 1 for a perpendicular approach ($\gamma_\lambda = 90°$) of the H atom to the H_2 molecule; (d) corresponding contours for ε_2^{ad}. All contour energies shown are in eV and correspond to the DSP fit to *ab initio* energies described in Ref. 18. The dashed lines in panels (c) and (d) correspond to conical intersection geometries.

γ^{DMBE} has a maximum where γ has a minimum and vice versa. For all other ρ, it shows the qualitatively correct behavior but with the absolute value of its maximum (or minimum) always smaller than that of γ. Also, for all ρ, the agreement between γ^{DMBE} and γ gets worse as θ is increased. To make this comparison more quantitative, we display in Fig. 7 the quantity $\Delta_\gamma(\rho,\theta)$ defined by Eq. (56) as a function of θ for fixed values of ρ. As expected, γ^{DMBE} agrees in general with the present optimal γ only close to the conical intersection ($\theta = 0°$). In the vicinity of $\rho = 4$ bohr, this agreement is very good up to about $\theta = 30°$. This analysis shows that even if the transverse part of the *ab initio* first-derivative coupling is ignored, as was done in the DMBE treatment,[47] γ^{DMBE} and hence β^{DMBE} agrees with the current γ only in the vicinity of the conical intersection, as expected, and should not be used to construct diabatic states and nuclear wave functions for accurate two-electronic-state scattering calculations.

Figure 8 displays the γ_{6D} obtained from the Poisson equation solution using only Dirichlet boundary conditions. Comparison of panels (a)–(d) of this figure with the corresponding panels of Fig. 5 shows that the maximum magni-

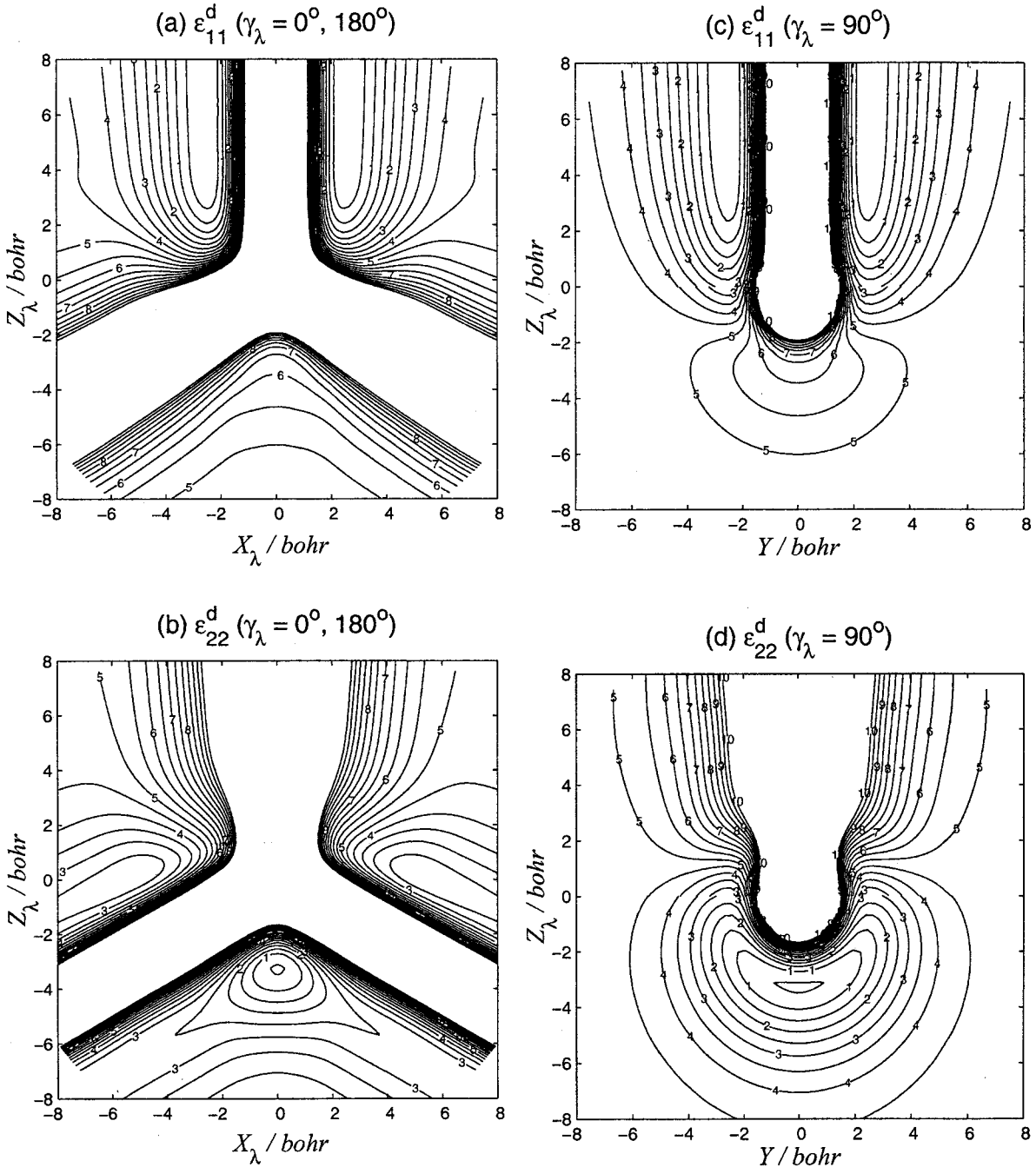

FIG. 14. Same as for Fig. 13 except that the displayed energy contours correspond to the diagonal diabatic energies ε^{d}_{11} and ε^{d}_{22}.

tude of γ_{6D} is on average half that of the optimal γ. This can be qualitatively explained by the fact that γ_{6D} is made to be zero at all six boundaries and hence it does not increase enough in magnitude inside the enclosed region to become smaller than the corresponding optimal γ. In addition, the maxima and minima in γ_{6D} occur in the same ϕ_λ regions as those of the corresponding optimal γ. Comparing the contours of γ_{6D} [Fig. 8 panels (e)–(h)] with those of the optimal γ [Fig. 5 panels (e)–(h)] highlights the qualitative similarity in the sharp rises around $\phi_\lambda = 60°$, 180°, and 300°.

As mentioned in Sec. III B, Fig. 9 displays the longitudinal part [$\mathbf{w}^{(1)ad}_{lon}$] of the first-derivative coupling vector for $\rho = 4$, 6, and 8 bohr. It has four sets of panels: (a) $\theta = 1°$ (triatomic geometries near the conical intersection), (b) $\theta = 30°$, (c) $\theta = 60°$, and (d) $\theta = 90°$ (collinear triatomic geometries). Figure 10 displays the corresponding plots for the transverse part ($\mathbf{w}^{(1)ad}_{tra}$) of that coupling vector.

The panels in the leftmost column of Fig. 9 depict the $\mathbf{w}^{(1)ad}_{lon}$ vector for $\rho = 4$ bohr, which is expected to be of high dynamical importance for the $H+H_2$ reaction. For the $\theta = 1°$ case [Fig. 9(a), $\rho = 4$ bohr], the longitudinal vector has a magnitude of about $5\,\text{bohr}^{-1}$ and a negligible z-component, translating into a strong dominance of its ϕ_λ-component near the conical intersection. The adiabatic energies (E_1 and E_2, see Fig. 5 in Ref. 18) are comparable to each other and stay around 3.6 eV in this region. At θ

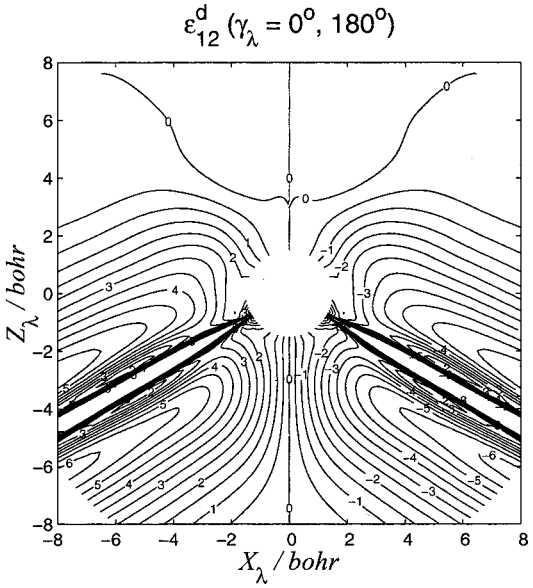

FIG. 15. Contours corresponding to the off-diagonal diabatic energy ε_{12}^{d} in the $X_\lambda Z_\lambda$ plane of Fig. 1 for a collinear approach ($\gamma_\lambda = 0°$ or 180°) of the H atom to the H_2 molecule. All contour energies shown are in eV.

$=30°$ [Fig. 9(b), $\rho=4$ bohr], values of E_1 as low as 1.5 eV occur, E_2 is 5 eV or larger and $\mathbf{w}_{\text{lon}}^{(1)\text{ad}}$ has a smaller magnitude than for the $\theta=1°$ case [Fig. 9(a), $\rho=4$ bohr]. At $\theta=60°$ [Fig. 9(c), $\rho=4$ bohr], values of E_1 as low as 0.25 eV occur, E_2 is 6 eV or larger, and $\mathbf{w}_{\text{lon}}^{(1)\text{ad}}$ shows a sharper variation with ϕ_λ than before [Fig. 9(b), $\rho=4$ bohr] around $\phi_\lambda=60°$, 180°, and 300°. At $\theta=90°$ [Fig. 9(d), $\rho=4$ bohr], which corresponds to collinear geometries, E_1 energies as low as 0.2 eV occur and this PES varies more rapidly with ϕ_λ than for the smaller values of θ, and E_2 is again 6 eV or larger. $\mathbf{w}_{\text{lon}}^{(1)\text{ad}}$ is comparable to the $\theta=60°$ case. For the $\rho=6$ bohr (panels in the central column of Fig. 9) and 8 bohr (panels in the rightmost column of Fig. 9) cases, which correspond to triatomic large sized geometries, the electronic energies as well as the longitudinal vectors have general characteristics that are analogous to the $\rho=4$ bohr case. In both these cases, E_1 energies as low as 0.2 eV occur and $\mathbf{w}_{\text{lon}}^{(1)\text{ad}}$ has comparable or larger magnitudes with maxima around $\phi_\lambda=60°$, 180°, and 300°.

The panels in the leftmost column of Fig. 10 display $\mathbf{w}_{\text{tra}}^{(1)\text{ad}}$, the transverse part of the coupling vector for $\rho=4$ bohr, where we observe very small absolute magnitudes near the conical intersection [$\theta=1°$, Fig. 10(a)]. For this value of ρ, as we move away from the conical intersection, the magnitude of $\mathbf{w}_{\text{tra}}^{(1)\text{ad}}$ increases to between 0.05 bohr^{-1} and 0.1 bohr^{-1}. There is also an initial increase [up to around $\theta=60°$, Fig. 10(c)] and a final decrease in the relative magnitude of its z-component. The θ-component [$w_{\text{tra},\theta}^{(1)\text{ad}}$] of the transverse coupling vector at $\theta=90°$ should be zero [due to the Neumann condition imposed at this boundary by Eq. (47)]. This should manifest itself in the z-component of the transverse vector being zero [due to Eq. (57)]. Figure 10 panel (d) (for $\rho=4$ bohr) shows that it is close to zero (less than 0.001 bohr^{-1}) everywhere except at $\phi_\lambda=0°$, 120°, and 240°, where it is of the order of 0.030 bohr^{-1}. This is due to

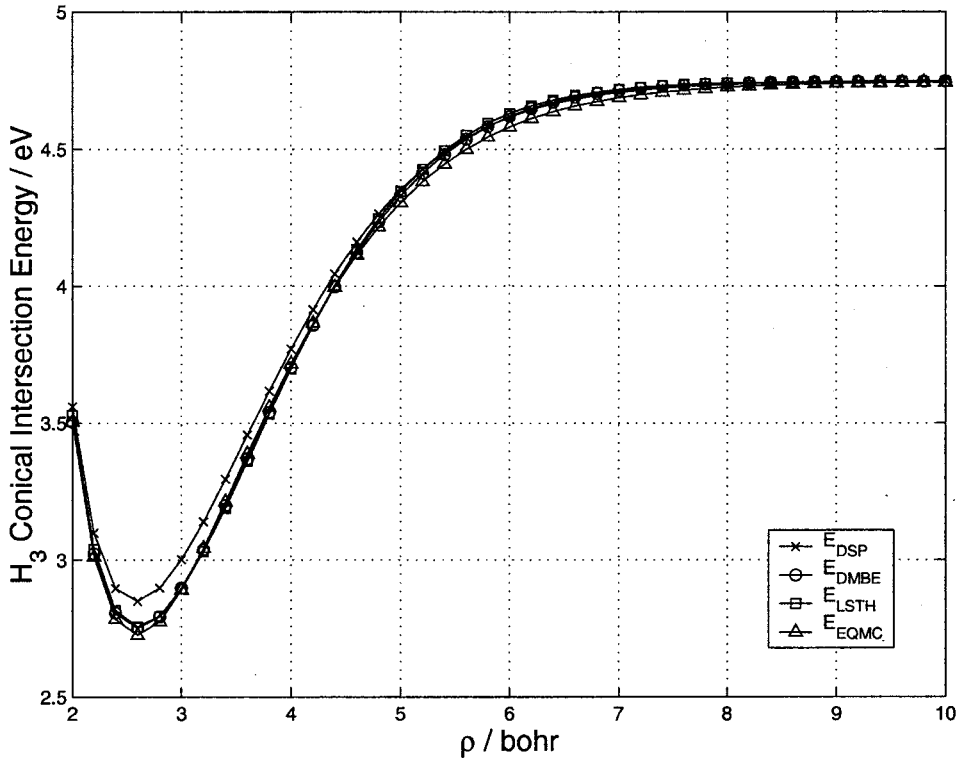

FIG. 16. Conical intersection energies as a function of ρ for DSP (crosses), DMBE (circles), LSTH (squares), and EQMC (triangles) PESs. The DSP curve corresponds to $Z_\lambda=0$ energies in panels (c) and (d) of Fig. 13.

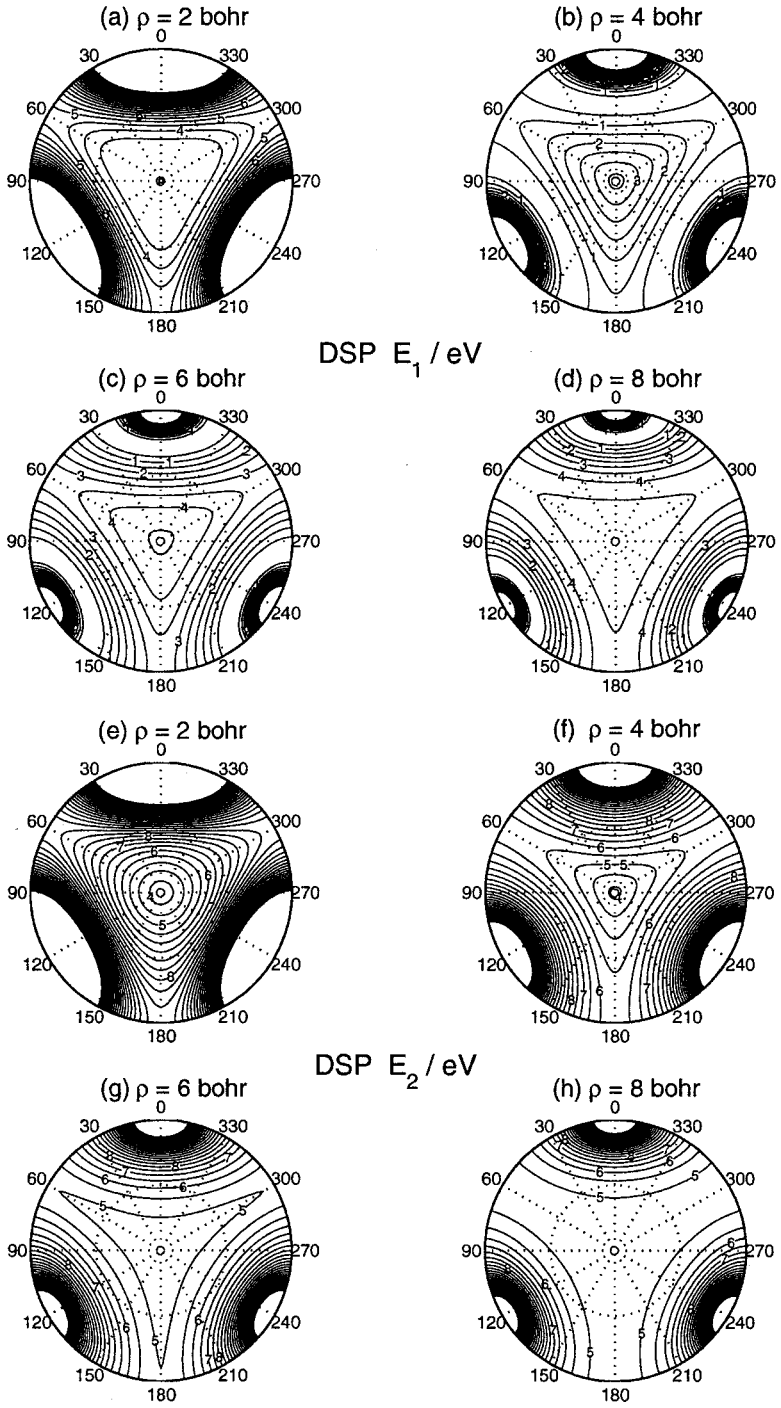

FIG. 17. Adiabatic ground state (E_1) energy contours in an equatorial view (see text for definition) for (a) $\rho=2$ bohr, (b) $\rho=4$ bohr, (c) $\rho=6$ bohr, and (d) $\rho=8$ bohr; and corresponding adiabatic first-excited state (E_2) energy contours for (e) $\rho=2$ bohr, (f) $\rho=4$ bohr, (g) $\rho=6$ bohr, and (h) $\rho=8$ bohr. All contour energies shown are in eV.

the Dirichlet boundary condition imposed on γ at $\phi_\lambda=0°$ [see Eq. (42)] and by symmetry at 120° and 240°. A look at the adiabatic energies in these regions (see Fig. 5 in Ref. 18) indicates that these energies remain higher than 10 eV in these regions, which will therefore not be accessible for scattering at or below 5 eV. For $\rho=6$ bohr (central column of Fig. 10) and $\rho=8$ bohr (rightmost column of Fig. 10), nothing unusual happens except for the fact that away from the conical intersection the magnitudes of $\mathbf{w}_{\text{tra}}^{(1)\text{ad}}$ increase to the $0.01\,\text{bohr}^{-1}$ to $0.02\,\text{bohr}^{-1}$ range.

A comparison of the transverse coupling vectors (Fig. 10) with their longitudinal counterparts (Fig. 9) leads to the following conclusions. For all hyperradii shown, the transverse vectors have similar magnitude x, y, and z components, where the x and y components are smaller in general than their longitudinal counterparts. Comparing Figs. 9(a) and 10(a) for $\rho=4$ bohr, both of which correspond to $\theta=1°$ (near-conical intersection geometries), the transverse (or *nonremovable*) vector is three orders of magnitude smaller than its longitudinal counterpart, a typical situation near the conical intersection. In sharp contrast, comparing Figs. 9(d) and 10(d) for this hyperradius, both of which correspond to $\theta=90°$ (collinear geometries), the magnitudes of the transverse and longitudinal vectors are similar to each other but at least an order of magnitude smaller than the magnitude of the longitudinal vector near the conical inter-

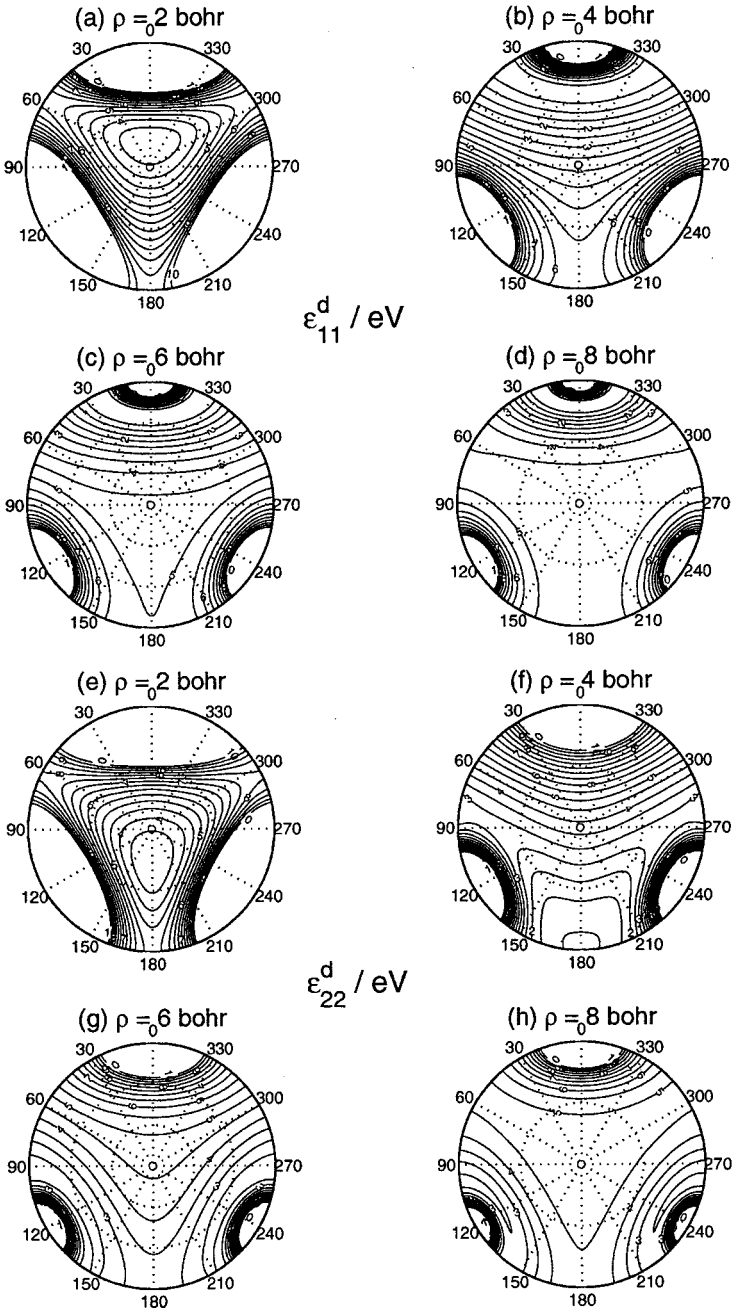

FIG. 18. Same as for Fig. 17 except that the displayed energy contours correspond to the diagonal diabatic energies ε_{11}^{d} and ε_{22}^{d}.

section. These conclusions are valuable due to the dynamical importance of the region around $\rho=4$ bohr. Near the conical intersection ($\theta=1°$), the ground (E_1) and first-excited (E_2) adiabatic PESs are very close to each other (see Fig. 5 in Ref. 18), so one expects that there will be maximum hopping of the nuclei between these PESs. In this region, the transverse (*nonremovable*) part is quite small (around $0.005\,\mathrm{bohr}^{-1}$ or less) and so this part is expected to have only a small effect on the reactive scattering. Near the collinear geometry regions, $\theta=90°$, the E_1 and E_2 adiabatic PESs are separated by around 5 eV, so although the transverse vector is not that much smaller than the longitudinal vector, the separation between the surfaces is big enough that it should prevent any noticeable hopping of nuclei from one surface to the other. The same analysis for $\rho=6$ bohr and 8 bohr leads to similar conclusions. The main points of difference are as follows. As we go from the conical intersection region, $\theta=1°$, to the collinear region, $\theta=90°$, the transverse vector remains at least an order of magnitude smaller than the longitudinal vector, whenever the two surfaces are closer than 5 eV. The transverse part becomes comparable to the longitudinal part only in regions where the two surfaces are separated by 5 eV or more.

Figure 11 depicts the transverse vector $\mathbf{w}_{\mathrm{tra},6D}^{(1)\mathrm{ad}}$ obtained by the all-Dirichlet Poisson equation calculation $\mathbf{b}_2$ described in Sec. II D. Its leftmost column ($\rho=4$ bohr) compared with the optimal $\mathbf{w}_{\mathrm{tra}}^{(1)\mathrm{ad}}$ (leftmost column of Fig. 10) shows that the magnitudes of the former are 2 to 4 times those of the latter. The middle column of Fig. 11 ($\rho=6$ bohr), compared

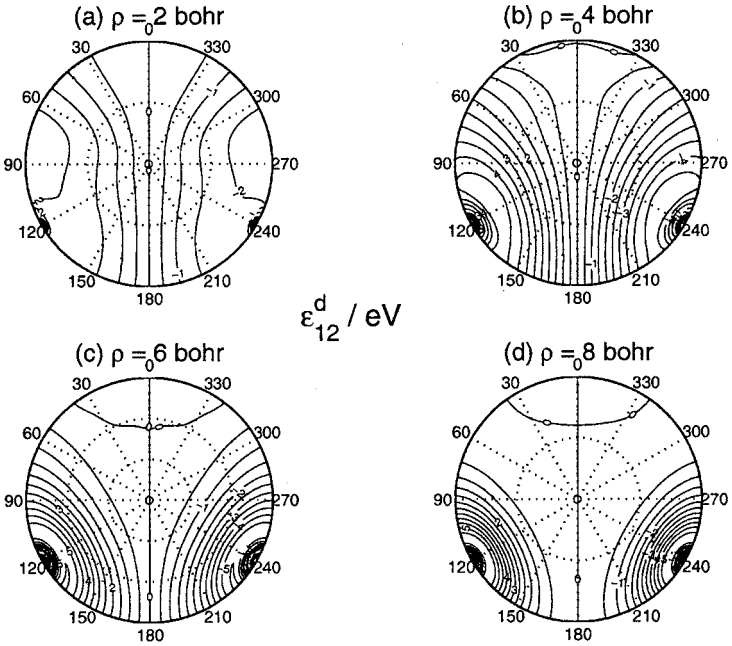

FIG. 19. Contours corresponding to the off-diagonal diabatic energy ε_{12}^{d} in the equatorial view for (a) $\rho=2$ bohr, (b) $\rho=4$ bohr, (c) $\rho=6$ bohr, and (d) $\rho=8$ bohr.

with the corresponding column of Fig. 10, shows that $\mathbf{w}_{\mathrm{tra},6D}^{(1)\mathrm{ad}}$ is 5–10 times larger in magnitude than $\mathbf{w}_{\mathrm{tra}}^{(1)\mathrm{ad}}$. A similar comparison of the rightmost column ($\rho=8$ bohr) shows its magnitude to be 10–50 times larger than that of the optimal $\mathbf{w}_{\mathrm{tra}}^{(1)\mathrm{ad}}$ vector. To make this comparison quantitative over the full domain U we evaluated, using Eq. (54), the average magnitude of both transverse parts and found them to be $0.0208\,\mathrm{bohr}^{-1}$ for the optimal transverse vector and $0.0981\,\mathrm{bohr}^{-1}$ for the full-Dirichlet $\mathbf{w}_{\mathrm{tra},6D}^{(1)\mathrm{ad}}$ transverse vector, resulting in a value of the ratio defined by Eq. (55) of $\xi_2=4.7$, i.e., the $\mathbf{w}_{\mathrm{tra},6D}^{(1)\mathrm{ad}}$ vector is in average nearly five times larger than the optimal one. This shows that the minimization provided by the three-Neumann boundary conditions of the optimal calculation $\mathbf{b}_0$ is very significant. Since it is the transverse part that is retained in the diabatic equations describing the nuclear motion, and has been minimized over the entire important domain U of nuclear configuration space, it will be interesting to determine by a perturbative treatment how and in what regions of that space it will affect the scattering dynamics for the H_3 system at energies of the order of 5 eV and below.

The values of the $\langle \mathrm{w}_{\mathrm{tra}}^{(1)\mathrm{ad}}\rangle_i$ for the calculations $\mathbf{b}_3$ through $\mathbf{b}_8$ were $0.0856\,\mathrm{bohr}^{-1}$, $0.0236\,\mathrm{bohr}^{-1}$, $0.0683\,\mathrm{bohr}^{-1}$, $0.0863\,\mathrm{bohr}^{-1}$, $0.0978\,\mathrm{bohr}^{-1}$, and $0.0687\,\mathrm{bohr}^{-1}$, respectively, resulting in corresponding values of ξ_i of 4.1, 1.1, 3.3, 4.1, 4.7, and 3.3. Two important conclusions are:

(a) the $\mathbf{b}_4$ calculation (Neumann conditions on S_4 and S_6 and Dirichlet conditions $\gamma=0$ at other S_i) is almost as good as the optimal $\mathbf{b}_0$ calculation;
(b) the order of importance of using Neumann boundary conditions to minimize $\langle \mathrm{w}_{\mathrm{tra}}^{(1)\mathrm{ad}}\rangle$ is S_6 first, followed by S_4 and S_5.

Figure 12 shows the longitudinal $\Phi_{\mathrm{lon}}(\phi_\lambda;\rho,\theta)$ and transverse $\Phi_{\mathrm{tra}}(\phi_\lambda;\rho,\theta)$ open path phases as a function of ϕ_λ for four values of θ and four values of ρ evaluated using Eqs. (60) and (61). For the $\theta=1°$ case, to a very good approximation (0.2% or smaller difference) Φ_{lon} is equal to $\phi_\lambda/2$ for all the values of ρ considered. This is clearly expected because this value of θ corresponds to a region of configuration space very close to the conical intersection and $\phi_\lambda/2$ is a major part of the diabatization angle β, γ being very small in that region. For other values of θ, Φ_{lon} fluctuates around this $\phi_\lambda/2$ value and returns to it at regular intervals of 60° in ϕ_λ. As a result, we can approximate Φ_{lon} by a sum of two terms, the first one being $\phi_\lambda/2$ and the second more complicated one possessing the P_3 symmetry (of H_3) via a $\sin 3\phi_\lambda$ dependence. This second term is the γ term of the diabatization angle β given by Eq. (35), since from Eqs. (13) and (60) we have $\Phi_{\mathrm{lon}}\equiv\beta$. The fluctuations in Φ_{lon} about $\phi_\lambda/2$ are due to this second term and have an amplitude which increases monotonically with ρ between $\rho=2$ bohr and $\rho=8$ bohr. This seems to stem from the fact that for a large value of ρ, the length of the circular loop around the conical intersection is large, which leads to a large phase accumulation in these fluctuations. As mentioned in Sec. III B, the corresponding topological phases (closed-loop line integrals, $\Phi_{\mathrm{T,lon}}$) can be read off these panels by looking at the value of Φ_{lon} at $\phi_\lambda=2\pi$. It can be seen that for all values of ρ and θ considered in Fig. 12 [panels (a)–(d)], $\Phi_{\mathrm{T,lon}}=\pi$, satisfying the condition given by Eq. (25) for $p=1$ since we are encircling only one conical intersection, the one between the $1\,^2A'$ and $2\,^2A'$ electronic states of H_3.

The transverse open path phase $\Phi_{\mathrm{tra}}(\phi_\lambda;\rho,\theta)$ was evaluated as a function of ϕ_λ by using both the middle part and the right-hand side of Eq. (61) for the same four values each of ρ and θ, used for Φ_{lon}. Both evaluations give identical results, which is shown in panels (e)–(h) of Fig. 12. This again is consistent with the fact that we are encircling one conical intersection. For the $\theta=1°$ case, Φ_{tra} is nearly

zero, which is expected due to the dominance of $\mathbf{w}_{\mathrm{lon}}^{(1)\mathrm{ad}}$ over $\mathbf{w}_{\mathrm{tra}}^{(1)\mathrm{ad}}$ in this region close to the conical intersection. In general, for each θ, Φ_{tra} is the sum of a linear term in ϕ_λ, whose slope can be positive, negative or zero, plus an oscillatory term of period $2\pi/3$. Also, the corresponding topological phases $\Phi_{\mathrm{T,tra}}$ (Φ_{tra} at $\phi_\lambda=2\pi$) show a value close to zero not only for $\theta=1°$ and all four values of ρ, but also for $\theta=90°$ (i.e., collinear geometries) at $\rho=4$ bohr. Examination of the $\mathbf{w}_{\mathrm{tra}}^{(1)\mathrm{ad}}$ vector (Fig. 10) at these geometries, shows that its magnitude is comparable to its value at other geometries where $\Phi_{\mathrm{T,tra}}$ is significantly different from zero. We conclude that the vanishing of $\Phi_{\mathrm{T,tra}}$ is a necessary but insufficient condition for the the first-derivative coupling vector to be purely longitudinal.

Using the diabatization angle β obtained as described in Sec. III A and discussed in the first two paragraphs of the present section, and the adiabatic ground and first-excited DSP PESs obtained previously,[18] we have calculated, using Eq. (65), the diagonal and off-diagonal elements of the diabatic energy matrix $\boldsymbol{\varepsilon}^d$. Figure 13 shows the cuts of the adiabatic ground ($\varepsilon_1^{\mathrm{ad}}$) and first-excited ($\varepsilon_2^{\mathrm{ad}}$) PESs with the $X_\lambda Z_\lambda$ and YZ_λ planes as explained in Sec. III C. Panels (a)–(b) correspond to collinear configurations and show the three atom–diatom channels. For such configurations, the lowest value of $\varepsilon_1^{\mathrm{ad}}$ is 0.013 eV (close to the $H+H_2$ limit) and that of $\varepsilon_2^{\mathrm{ad}}$ is 4.62 eV (close to the H+H+H limit). In addition, since the intersection between these two PESs occurs for equilateral triangle ($\theta=0°$) geometries, the collinear ($\theta=90°$) cuts of these panels do not intersect. Panels (c) and (d) correspond to perpendicular configurations, which for $Z_\lambda=0$ are equilateral triangles and hence conical intersection configurations. Therefore, the dashed horizontal lines in these panels (at $Z_\lambda=0$) correspond to the conical intersection lines for which $\varepsilon_1^{\mathrm{ad}}=\varepsilon_2^{\mathrm{ad}}$. The minimum value of this conical intersection energy for the DSP PESs (Ref. 18) also used in the present calculation is 2.85 eV and occurs for $\rho=Y=2.6$ bohr. The corresponding point is located in panel (d) inside the 3 eV contour. The hyperspherical coordinates don't span negative values of Y, but these are nevertheless included for display convenience. The highest energy contour for $\varepsilon_1^{\mathrm{ad}}$ depicted in panel (c) is for 2.4 eV and the lowest energy contour for $\varepsilon_2^{\mathrm{ad}}$ depicted in panel (d) is for 3.0 eV. The conical intersection energies [corresponding to $Z_\lambda=0$ in panels (c) and (d)] are displayed in Fig. 16 as a function of ρ for the DSP, DMBE, LSTH, and EQMC PESs. The minima of the latter three are 2.75, 2.76, and 2.73 eV, respectively. The minimum DSP conical intersection energy of 2.85 eV mentioned above is slightly higher than that for the latter three PESs. This is due to the fact that the *ab initio* electronic energies used for fitting the DSP PESs resulted from calculations performed to obtain good energies for both the ground and first-excited state. This leads to a slightly higher DSP energy than it would be, if the basis set used was chosen to optimize the ground state energies only.[18]

Fig. 14 depicts the diagonal elements (ε_{11}^d and ε_{22}^d) of the diabatic energy matrix on the same cuts as Fig. 13. For the collinear configurations [panels (a) and (b)], the lowest ε_{11}^d and ε_{22}^d contours displayed are for 0.5 eV but are located in different regions of the internal configuration space. The ε_{11}^d minimum occurs in the positive Z_λ region for some values of X_λ at which the $\varepsilon_1^{\mathrm{ad}}$ contours also show a minimum. The ε_{22}^d minimum however occurs in the negative Z_λ region for some values of X_λ at which $\varepsilon_1^{\mathrm{ad}}$ contours also show a minimum. Interestingly, the saddle point at $X_\lambda=0$ in $\varepsilon_1^{\mathrm{ad}}$ [Fig. 13(a)] transforms to a well roughly 2.0 eV deep for ε_{22}^d. The behavior of ε_{11}^d in this region is very similar to that of $\varepsilon_2^{\mathrm{ad}}$ [Fig. 13(b)]. The ε_{11}^d and ε_{22}^d PESs display an intersection for collinear geometries at about 4.5 eV. No intersection is present for such geometries between the $\varepsilon_1^{\mathrm{ad}}$ and $\varepsilon_2^{\mathrm{ad}}$ PESs. For the perpendicular configurations [panels (c) and (d)], the relation of ε_{11}^d and ε_{22}^d with $\varepsilon_1^{\mathrm{ad}}$ and $\varepsilon_2^{\mathrm{ad}}$ is similar to that for the collinear case. Also for these configurations, the ε_{11}^d and ε_{22}^d PESs display an intersection at around 2.85 eV, similar to the one between the adiabatic PESs. Figure 15 shows the off-diagonal element ε_{12}^d of the diabatic energy matrix for collinear configurations. This element vanishes for perpendicular configurations. From Eqs. (65) and (35) it can be easily shown that in general ε_{12}^d is antisymmetric with respect to $\phi_\lambda=0°$ and $\phi_\lambda=180°$, i.e., the YZ_λ plane, for which $X_\lambda=0$. Figure 15 corresponds to $Y=0$. As a result, this antisymmetry manifests itself in that figure with respect to the $X_\lambda=0$ axis. This translates into ε_{12}^d being attractive for $X_\lambda>0$ and repulsive for $X_\lambda<0$. Since ε_{12}^d is of the same order of magnitude as ε_{11}^d and ε_{22}^d and it is the largest term that couples the two nuclear motion scattering equations in the two-electronic-state diabatic representation of Eq. (19), it should be of major importance for the dynamics of the $H+H_2$ reaction at energies for which the two PESs participate.

Fig. 17 displays the adiabatic PESs in equatorial views for four values of the hyperradii ρ (2, 4, 6, and 8 bohr). These PESs have been discussed previously[18] and are repeated here only for comparison with the corresponding views of the diabatic PESs. Figure 18 depicts the diagonal ε_{11}^d and ε_{22}^d PESs in the equatorial view for the same four values of ρ. The P_3 symmetry of the adiabatic PESs is lost in the diabatic representation due to the $\phi_\lambda/2$ term in β [see Eq. (35)] which does not have the required $3\phi_\lambda$ dependence. For $\rho=2$ bohr, the lowest contour displayed for both the ε_{11}^d and ε_{22}^d PESs is the 3.5 eV contour. For $\rho=4$ bohr, 6 bohr and 8 bohr it is the 0.5 eV contour. A close look at all panels in Fig. 18 indicates that the top half circle of ε_{11}^d looks like $\varepsilon_1^{\mathrm{ad}}$ and the bottom half looks like $\varepsilon_2^{\mathrm{ad}}$. Similarly, the top half of ε_{22}^d looks like $\varepsilon_2^{\mathrm{ad}}$ and the bottom half looks like $\varepsilon_1^{\mathrm{ad}}$. This is closely related to the discussion involving Fig. 4, where for the $\phi_\lambda=0°$ line (lying in the top half circle) β equals 0° making $\varepsilon_{11}^d=\varepsilon_1^{\mathrm{ad}}$ and $\varepsilon_{22}^d=\varepsilon_2^{\mathrm{ad}}$ and for the $\phi_\lambda=180°$ line (lying in the bottom half circle) β equals 90° which makes $\varepsilon_{11}^d=\varepsilon_2^{\mathrm{ad}}$ and $\varepsilon_{22}^d=\varepsilon_1^{\mathrm{ad}}$. Figure 19 shows the off-diagonal ε_{12}^d term of the diabatic energy matrix in an equatorial view for the same four values of ρ. As in Fig. 15, the contours are antisymmetric with respect to the $\phi_\lambda=0°,180°$ (i.e., the YZ_λ plane), one half of the ε_{12}^d PES being repulsive and the other half attractive. It displays a large flat region of 0 eV around the $\phi_\lambda=0°,180°$ lines suggesting negligible coupling in these regions. It will be interesting to see how this antisymmetric property of ε_{12}^d affects the scattering dynamics in such regions for energies of interest (less than 5 eV).

We conclude, from the discussion in this section, that neglecting the transverse (*nonremovable*) part of $\mathbf{w}^{(1)\mathrm{ad}}$ in the diabatic nuclear Schrödinger equation should, as is usually assumed, but especially for the optimal adiabatization described in this paper, be a good approximation in the first step of an accurate two-state scattering calculation. As we have already computed this nonremovable part, we can add it as a perturbation to the scattering results in a second step and thereby assess just how good this approximation really is. Use of the global optimal diabatic basis reported here is underway in the implementation of a two-electronic-state scattering calculation for H_3.

IV. SUMMARY AND CONCLUSIONS

We have reported the first global optimal diabatic basis, obtained from accurate *ab initio* first-derivative couplings between the $1\,^2A'$ and $2\,^2A'$ adiabatic PESs of H_3. These couplings were used in a three-dimensional Poisson equation for the diabatization angle, over the entire dynamically important domain U of internal nuclear configuration space, together with a combination of Neumann and Dirichlet boundary conditions. These conditions were chosen so as to minimize the average value of the magnitude of the transverse (*nonremovable*) part of the first-derivative coupling vector over that domain. Since that is the only part of that vector that appears in the diabatic nuclear motion Schrödinger equation, the result is an optimal diabatic basis. The minimization was measured quantitatively by solving the Poisson equation with only Dirichlet boundary conditions and comparing the average magnitude of the transverse vector obtained from this solution with that obtained from the optimal solution. The former was found to be 4.7 times larger than the optimal one, indicating that the minimization provided by the Neumann boundary conditions used in the latter was very significant.

The diabatization angle was calculated over the full U domain. The resulting diagonal and off-diagonal components of the diabatic potential energy matrix were obtained and their importance for the reactive scattering process was discussed. The longitudinal and transverse parts of the full first-derivative coupling vector were calculated and a detailed analysis of their relative magnitudes in the dynamically important regions of nuclear configuration space was presented. In a first but good approximation to the nuclear motion diabatic scattering equations, the transverse part can be neglected (as well as the small second-derivative diabatic coupling matrix correction to the diabatic PESs). Since, however, it is now known, it can be introduced perturbatively at a later stage to assess its importance for the two-electronic-state scattering calculations. It is expected to have only a small effect on the scattering dynamics, but just how small remains to be determined.

ACKNOWLEDGMENTS

This work was supported in part by NSF Grant No. CHE 9810050. The authors thank Mr. Prashant Purohit for suggesting the derivation given in the Appendix.

APPENDIX: OPTIMAL BOUNDARY CONDITIONS FOR THE DIABATIZATION ANGLE POISSON EQUATION

Consider the Helmholtz decomposition of the first-derivative coupling vector $\mathbf{w}^{(1)\mathrm{ad}}(\mathbf{q})$ given by Eq. (28),

$$\mathbf{w}^{(1)\mathrm{ad}}(\mathbf{q}) = \boldsymbol{\nabla}_{\mathbf{q}}\beta(\mathbf{q}) + \mathbf{w}_{\mathrm{tra}}^{(1)\mathrm{ad}}(\mathbf{q}), \tag{A1}$$

where the diabatization angle $\beta(\mathbf{q})$ is the solution of the Poisson equation [Eq. (29)],

$$\nabla_{\mathbf{q}}^2\beta(\mathbf{q}) = \sigma(\mathbf{q}), \tag{A2}$$

the source term $\sigma(\mathbf{q})$ being defined by

$$\sigma(\mathbf{q}) = \nabla_{\mathbf{q}}\cdot\mathbf{w}^{(1)\mathrm{ad}}(\mathbf{q}). \tag{A3}$$

Let $\beta_0(\mathbf{q})$ and $\beta_1(\mathbf{q})$ be solutions of Eq. (A2) subject to boundary conditions specified by the functions $\mathrm{B}_0(\mathbf{q}_\mathsf{S})$, and $\mathrm{B}_1(\mathbf{q}_\mathsf{S})$ respectively and to be given in greater detail below. $\mathbf{q}_\mathsf{S}$ designates values of $\mathbf{q}$ on the boundary surface S that encloses the domain V in which Eq. (A2) is to be solved. In the symmetrized hyperspherical coordinates $\mathbf{q}$ $(\rho,\theta,\phi_\lambda)$, that domain is given by $\rho_{\min}\leqslant\rho\leqslant\rho_{\max}$, $\theta_{\min}\leqslant\theta\leqslant\theta_{\max}$ and $\phi_{\lambda\,\min}\leqslant\phi_\lambda\leqslant\phi_{\lambda\,\max}$. S is comprised of 6 parts S_i $(i=1-6)$ described in Sec. II D. Dirichlet conditions are used on the S_1, S_2, and S_3 parts of S for the reasons described after Eqs. (42), (44), and (45). As a result of these equations and Eq. (35) we have

$$\begin{aligned}
&\beta_0(\mathsf{S}_1)=0, \quad \beta_1(\mathsf{S}_1)=0,\\
&\beta_0(\mathsf{S}_2)=\pi/6, \quad \beta_1(\mathsf{S}_2)=\pi/6,\\
&\beta_0(\mathsf{S}_3)=\phi_\lambda/2, \quad \beta_1(\mathsf{S}_3)=\phi_\lambda/2.
\end{aligned} \tag{A4}$$

This leaves the three remaining boundary surfaces S_4 through S_6 on which Neumann, Dirichlet or mixed boundary conditions may be adopted.

Let us define a residue function $E(\beta(\mathbf{q}))$ that measures the square of the average magnitude of $\mathbf{w}_{\mathrm{tra}}^{(1)\mathrm{ad}}(\mathbf{q})$ over the domain V,

$$E(\beta(\mathbf{q})) = \int_{\mathsf{V}} [\mathbf{w}^{(1)\mathrm{ad}}(\mathbf{q}) - \boldsymbol{\nabla}_{\mathbf{q}}\beta(\mathbf{q})]^2 d\mathbf{q}. \tag{A5}$$

In addition, let

$$\Delta\beta(\mathbf{q}) = \beta_1(\mathbf{q}) - \beta_0(\mathbf{q}). \tag{A6}$$

We now impose the condition that $\beta_0(\mathbf{q})$ be the solution of the Poisson equation that minimizes the average value of $|\mathbf{w}_{\mathrm{tra}}^{(1)\mathrm{ad}}(\mathbf{q})|$ over V. This condition can be expressed as

$$\left\{\frac{\partial}{\partial\epsilon}E[\beta_0(\mathbf{q})+\epsilon\Delta\beta(\mathbf{q})]\right\}(\epsilon=0)=0. \tag{A7}$$

This minimization condition will result in a specification of the boundary function $\mathrm{B}_0(\mathbf{q}_\mathsf{S})$ and of the nature of the associated boundary condition (Neumann, Dirichlet or mixed), as described below.

In light of the Dirichlet conditions represented by Eqs. (A4), the quantity $\Delta\beta(\mathbf{q})$ is given by

$$\begin{aligned}
&\Delta\beta(\mathsf{S}_1)=0,\\
&\Delta\beta(\mathsf{S}_2)=0,
\end{aligned} \tag{A8}$$

$$\Delta\beta(\mathsf{S}_3)=0,$$

on the two ϕ_λ boundary surfaces S_1 and S_2 and the minimum θ boundary surface S_3. Replacement of Eq. (A5) into Eq. (A7) results in

$$\left\{\frac{\partial}{\partial\epsilon}\int_{\mathsf{V}}[\mathbf{w}^{(1)\mathrm{ad}}(\mathbf{q})-\boldsymbol{\nabla}_{\mathbf{q}}\beta_0(\mathbf{q})-\epsilon\boldsymbol{\nabla}_{\mathbf{q}}\Delta\beta(\mathbf{q})]^2 d\mathbf{q}\right\}(\epsilon=0)=0. \tag{A9}$$

Since $\mathbf{q}$ and ϵ are independent variables, we can interchange the order of differentiation and integration in this expression to get

$$\int_{\mathsf{V}}[\mathbf{w}^{(1)\mathrm{ad}}(\mathbf{q})-\boldsymbol{\nabla}_{\mathbf{q}}\beta_0(\mathbf{q})]\cdot\boldsymbol{\nabla}_{\mathbf{q}}\Delta\beta(\mathbf{q})d\mathbf{q}=0. \tag{A10}$$

With the help of the identity

$$\mathbf{u}\cdot\boldsymbol{\nabla}_{\mathbf{q}}v=\boldsymbol{\nabla}_{\mathbf{q}}\cdot(v\mathbf{u})-v(\boldsymbol{\nabla}_{\mathbf{q}}\cdot\mathbf{u}). \tag{A11}$$

where v and $\mathbf{u}$ are arbitrary scalar and vector functions of $\mathbf{q}$, Eq. (A10) furnishes

$$\int_{\mathsf{V}}\boldsymbol{\nabla}_{\mathbf{q}}\cdot\{\Delta\beta(\mathbf{q})[\mathbf{w}^{(1)\mathrm{ad}}(\mathbf{q})-\boldsymbol{\nabla}_{\mathbf{q}}\beta_0(\mathbf{q})]\}d\mathbf{q}-\int_{\mathsf{V}}\Delta\beta(\mathbf{q})\times[\boldsymbol{\nabla}_{\mathbf{q}}\cdot\mathbf{w}^{(1)\mathrm{ad}}(\mathbf{q})-\nabla^2_{\mathbf{q}}\beta_0(\mathbf{q})]d\mathbf{q}=0. \tag{A12}$$

Using the Gauss divergence theorem in the first term and Eq. (A3) in the second term of this equation we get

$$\int_{\mathsf{S}}\Delta\beta(\mathbf{q})[\mathbf{w}^{(1)\mathrm{ad}}(\mathbf{q})-\boldsymbol{\nabla}_{\mathbf{q}}\beta_0(\mathbf{q})]\cdot d\mathbf{s}-\int_{\mathsf{V}}\Delta\beta(\mathbf{q})[\sigma(\mathbf{q})-\nabla^2_{\mathbf{q}}\beta_0(\mathbf{q})]d\mathbf{q}=0, \tag{A13}$$

where the integral over the boundary surface S is the sum of six individual integrals evaluated on the six boundary surfaces $\mathsf{S}_i, i=1-6$. The quantity inside square brackets in the second term of Eq. (A13) is equal to zero since $\beta_0(\mathbf{q})$ is a solution of the Poisson equation [Eq. (A2)]. We now expand the surface integral in the first term of that equation and write

$$I(\mathsf{S})=\int_{\mathsf{S}}\Delta\beta(\mathbf{q})[\mathbf{w}^{(1)\mathrm{ad}}(\mathbf{q})-\boldsymbol{\nabla}_{\mathbf{q}}\beta_0(\mathbf{q})]\cdot d\mathbf{s}=\sum_{i=1}^{6}I(\mathsf{S}_i)=0, \tag{A14}$$

where

$$I(\mathsf{S}_i)=\int_{\mathsf{S}_i}\Delta\beta(\mathbf{q}_{\mathsf{S}_i})[\mathbf{w}^{(1)\mathrm{ad}}(\mathbf{q}_{\mathsf{S}_i})-\boldsymbol{\nabla}_{\mathbf{q}}\beta_0(\mathbf{q}_{\mathsf{S}_i})]\cdot d\mathbf{s}_i \tag{A15}$$

are the surface integrals of interest on the six parts of the closed surface S. They can be expressed as

$$I(\mathsf{S}_1)=-\int_{\rho_{\min}}^{\rho_{\max}}\int_{\theta_{\min}}^{\theta_{\max}}\Delta\beta(\mathsf{S}_1)\left[\mathrm{w}^{(1)\mathrm{ad}}_{\phi_\lambda}(\rho,\theta,\phi_{\lambda\,\min})-\left(\frac{1}{\rho\sin\theta}\frac{\partial\beta_0(\mathbf{q})}{\partial\phi_\lambda}\right)_{\phi_{\lambda\,\min}}\right]\rho\,d\rho d\theta, \tag{A16}$$

$$I(\mathsf{S}_2)=\int_{\rho_{\min}}^{\rho_{\max}}\int_{\theta_{\min}}^{\theta_{\max}}\Delta\beta(\mathsf{S}_2)\left[\mathrm{w}^{(1)\mathrm{ad}}_{\phi_\lambda}(\rho,\theta,\phi_{\lambda\max})-\left(\frac{1}{\rho\sin\theta}\frac{\partial\beta_0(\mathbf{q})}{\partial\phi_\lambda}\right)_{\phi_{\lambda\,\max}}\right]\rho\,d\rho d\theta, \tag{A17}$$

$$I(\mathsf{S}_3)=-\int_{\rho_{\min}}^{\rho_{\max}}\int_{\phi_{\lambda\,\min}}^{\phi_{\lambda\,\max}}\Delta\beta(\mathsf{S}_3)\left[\mathrm{w}^{(1)\mathrm{ad}}_{\theta}(\rho,\theta_{\min},\phi_\lambda)-\left(\frac{1}{\rho}\frac{\partial\beta_0(\mathbf{q})}{\partial\theta}\right)_{\theta_{\min}}\right]\rho\sin\theta_{\min}\,d\rho d\phi_\lambda, \tag{A18}$$

$$I(\mathsf{S}_4)=\int_{\rho_{\min}}^{\rho_{\max}}\int_{\phi_{\lambda\,\min}}^{\phi_{\lambda\,\max}}\Delta\beta(\mathsf{S}_4)\left[\mathrm{w}^{(1)\mathrm{ad}}_{\theta}(\rho,\theta_{\max},\phi_\lambda)-\left(\frac{1}{\rho}\frac{\partial\beta_0(\mathbf{q})}{\partial\theta}\right)_{\theta_{\max}}\right]\rho\sin\theta_{\max}\,d\rho d\phi_\lambda, \tag{A19}$$

$$I(\mathsf{S}_5)=-\int_{\theta_{\min}}^{\theta_{\max}}\int_{\phi_{\lambda\,\min}}^{\phi_{\lambda\max}}\Delta\beta(\mathsf{S}_5)\left[\mathrm{w}^{(1)\mathrm{ad}}_{\rho}(\rho_{\min},\theta,\phi_\lambda)-\left(\frac{\partial\beta_0(\mathbf{q})}{\partial\rho}\right)_{\rho_{\min}}\right]\rho^2_{\min}\sin\theta\,d\theta d\phi_\lambda, \tag{A20}$$

$$I(\mathsf{S}_6)=\int_{\theta_{\min}}^{\theta_{\max}}\int_{\phi_{\lambda\,\min}}^{\phi_{\lambda\max}}\Delta\beta(\mathsf{S}_6)\left[\mathrm{w}^{(1)\mathrm{ad}}_{\rho}(\rho_{\max},\theta,\phi_\lambda)-\left(\frac{\partial\beta_0(\mathbf{q})}{\partial\rho}\right)_{\rho_{\max}}\right]\rho^2_{\max}\sin\theta\,d\theta d\phi_\lambda. \tag{A21}$$

Because of the Dirichlet conditions on S_1, S_2, and S_3 that resulted in Eqs. (A8), $I(\mathsf{S}_1)$, $I(\mathsf{S}_2)$, and $I(\mathsf{S}_3)$ vanish. Equation (A14) requires that the sum of the remaining $I(\mathsf{S}_i)$ terms should vanish. Given the arbitrariness of the $\Delta\beta(\mathsf{S}_i)$ for $i=4-6$, in order for that to happen, it is necessary that each of its terms vanish. This results in

$$\left(\frac{\partial\beta_0(\mathbf{q})}{\partial\rho}\right)_{\rho_{\min}}=\mathrm{w}^{(1)\mathrm{ad}}_{\rho}(\rho_{\min},\theta,\phi_\lambda), \tag{A22}$$

$$\left(\frac{\partial\beta_0(\mathbf{q})}{\partial\rho}\right)_{\rho_{\max}}=\mathrm{w}^{(1)\mathrm{ad}}_{\rho}(\rho_{\max},\theta,\phi_\lambda), \tag{A23}$$

$$\left(\frac{\partial\beta_0(\mathbf{q})}{\partial\theta}\right)_{\theta_{\max}}=\rho\,\mathrm{w}^{(1)\mathrm{ad}}_{\theta}(\rho,\theta_{\max},\phi_\lambda). \tag{A24}$$

These are the Neumann boundary conditions used at the ρ and θ boundaries as described in Sec. II D in Eqs. (46)–(50). Together with Eqs. (A4) they specify the boundary functions $\mathrm{B}_0(\mathbf{q}_{\mathsf{S}})$ and the nature of the associated boundary conditions, as indicated after Eq. (A7). This physically acceptable choice of boundary conditions minimizes the average value of the magnitude of the coupling vector $\mathbf{w}^{(1)\mathrm{ad}}_{\mathrm{tra}}(\mathbf{q})$ over the important domain V and hence the extended domain U of internal nuclear configuration space.

[1] A. Kuppermann, in *Dynamics of Molecules and Chemical Reactions*, edited by R. E. Wyatt and J. Z. H. Zhang (Dekker, New York, 1996), pp. 411–472.
[2] M. Born, Nachr. Akad. Wiss. Gött. Math.-Phys. Kl. Article No. **6**, 1 (1951).
[3] M. Born and K. Huang, *Dynamical Theory of Crystal Lattices* (Oxford University Press, Oxford, 1954), pp. 166–177 and 402–407.
[4] H. C. Longuet-Higgins, Adv. Spectrosc. (N.Y.) **2**, 429 (1961).
[5] G. Herzberg and H. C. Longuet-Higgins, Discuss. Faraday Soc. **35**, 77 (1963).
[6] H. C. Longuet-Higgins, Proc. R. Soc. London, Ser. A **344**, 147 (1975).
[7] M. V. Berry, Proc. R. Soc. London, Ser. A **392**, 45 (1984).
[8] C. A. Mead, Chem. Phys. **49**, 23 (1980).
[9] C. A. Mead and D. G. Truhlar, J. Chem. Phys. **70**, 2284 (1979).
[10] B. Kendrick and R. T Pack, J. Chem. Phys. **104**, 7475 (1996).
[11] B. Kendrick and R. T Pack, J. Chem. Phys. **104**, 7502 (1996).
[12] R. J. Buenker, G. Hirsch, S. D. Peyerimhoff, P. J. Bruna, J. Römelt, M. Bettendorff, and C. Petrongolo, in *Current Aspects of Quantum Chemistry* (Elsevier, New York, 1981), pp. 81–97.
[13] M. Desouter-Lecomte, C. Galloy, J. C. Lorquet, and M. V. Pires, J. Chem. Phys. **71**, 3661 (1979).
[14] B. H. Lengsfield, P. Saxe, and D. R. Yarkony, J. Chem. Phys. **81**, 4549 (1984).
[15] P. Saxe, B. H. Lengsfield, and D. R. Yarkony, Chem. Phys. Lett. **113**, 159 (1985).
[16] B. H. Lengsfield and D. R. Yarkony, J. Chem. Phys. **84**, 348 (1986).
[17] J. O. Jensen and D. R. Yarkony, J. Chem. Phys. **89**, 975 (1988).
[18] R. Abrol, A. Shaw, A. Kuppermann, and D. R. Yarkony, J. Chem. Phys. **115**, 4640 (2001).
[19] P. M. Morse and H. Feshbach, *Methods of Theoretical Physics* (McGraw–Hill, New York, 1953), pp. 52–54, 1763.
[20] A. Thiel and H. Köppel, J. Chem. Phys. **110**, 9371 (1999).
[21] V. Sidis, in *State-Selected and State to State Ion–Molecule Reaction Dynamics: Part 2 Theory*, edited by M. Baer and C.-Y. Ng (Wiley, New York, 1992), Vol. 82, pp. 73–134.
[22] F. T. Smith, Phys. Rev. **179**, 111 (1969).
[23] M. Baer, Chem. Phys. Lett. **35**, 112 (1975).
[24] C. A. Mead and D. G. Truhlar, J. Chem. Phys. **77**, 6090 (1982).
[25] T. Pacher, L. S. Cederbaum, and H. Köppel, J. Chem. Phys. **89**, 7367 (1988).
[26] T. Pacher, C. A. Mead, L. S. Cederbaum, and H. Köppel, J. Chem. Phys. **91**, 7057 (1989).
[27] M. Baer and R. Englman, Mol. Phys. **75**, 293 (1992).
[28] K. Ruedenberg and G. J. Atchity, J. Chem. Phys. **99**, 3799 (1993).
[29] M. Baer and R. Englman, Chem. Phys. Lett. **265**, 105 (1997).
[30] M. Baer, J. Chem. Phys. **107**, 2694 (1997).
[31] B. K. Kendrick, C. A. Mead, and D. G. Truhlar, J. Chem. Phys. **110**, 7594 (1999).
[32] M. Baer, R. Englman, and A. J. C. Varandas, Mol. Phys. **97**, 1185 (1999).
[33] D. R. Yarkony, J. Chem. Phys. **112**, 2111 (2000).
[34] D. R. Yarkony, J. Chem. Phys. **105**, 10456 (1996).
[35] D. R. Yarkony, J. Phys. Chem. A **101**, 4263 (1997).
[36] N. Matsunaga and D. R. Yarkony, J. Chem. Phys. **107**, 7825 (1997).
[37] N. Matsunaga and D. R. Yarkony, Mol. Phys. **93**, 79 (1998).
[38] R. G. Sadygov and D. R. Yarkony, J. Chem. Phys. **109**, 20 (1998).
[39] D. R. Yarkony, J. Chem. Phys. **110**, 701 (1999).
[40] C. A. Mead, J. Chem. Phys. **72**, 3839 (1980).
[41] B. Lepetit and A. Kuppermann, Chem. Phys. Lett. **166**, 581 (1990).
[42] Y.-S. M. Wu, A. Kuppermann, and B. Lepetit, Chem. Phys. Lett. **186**, 319 (1991).
[43] Y.-S. M. Wu and A. Kuppermann, Chem. Phys. Lett. **201**, 178 (1993).
[44] A. Kuppermann and Y.-S. M. Wu, Chem. Phys. Lett. **205**, 577 (1993).
[45] Y.-S. M. Wu and A. Kuppermann, Chem. Phys. Lett. **235**, 105 (1995).
[46] A. Kuppermann and Y.-S. M. Wu, Chem. Phys. Lett. **241**, 229 (1995).
[47] A. J. C. Varandas, F. B. Brown, C. A. Mead, D. G. Truhlar, and N. C. Blais, J. Chem. Phys. **86**, 6258 (1987).
[48] M. Baer, Chem. Phys. **15**, 49 (1976).
[49] R. Englman, A. Yahalom, and M. Baer, Eur. Phys. J. D **8**, 1 (2000).
[50] R. Englman and M. Baer, J. Phys.: Condens. Matter **11**, 1059 (1999).
[51] A. Kuppermann, J. Phys. Chem. A **100**, 2621 (1996); **100**, 11202 (1996).
[52] A. Kuppermann, Chem. Phys. Lett. **32**, 374 (1975).
[53] L. M. Delves, Nucl. Phys. **9**, 391 (1959).
[54] L. M. Delves, Nucl. Phys. **20**, 275 (1960).
[55] D. Jepsen and J. O. Hirschfelder, Proc. Natl. Acad. Sci. U.S.A. **45**, 249 (1959).
[56] F. T. Smith, J. Math. Phys. **3**, 735 (1962).
[57] R. T. Ling and A. Kuppermann, in *Electronic and Atomic Collisions, Abstract of the 9th International Conference on the Physics of Electronic and Atomic Collisions*, Seattle, Washington, 24–30 July 1975, edited by J. S. Riley and R. Geballe (University of Washington Press, Seattle, 1975), Vol. 1, pp. 353–354.
[58] A. Kuppermann, in *Advances in Molecular Vibrations and Collision Dynamics*, edited by J. Bowman (JAI, Greenwich, 1994), Vol. 2B, pp. 117–186.
[59] Ref. 19, Eq. (1.4.8).
[60] J. C. Adams, Appl. Math. Comput. **43**, 79 (1991).
[61] J. C. Adams, Appl. Math. Comput. **34**, 113 (1989).
[62] S. Rogers, D. Wang, S. Walch, and A. Kuppermann, J. Phys. Chem. A **104**, 2308 (2000).
[63] Y.-S. M. Wu, A. Kuppermann, and J. B. Anderson, Phys. Chem. Chem. Phys. **6**, 929 (1999).
[64] B. Liu, J. Chem. Phys. **58**, 1925 (1973).
[65] P. Siegbahn and B. Liu, J. Chem. Phys. **68**, 2457 (1978).
[66] D. G. Truhlar and C. J. Horowitz, J. Chem. Phys. **68**, 2466 (1978); **71**, 1514(E) (1979).